THESIS FOR THE DEGREE OF DOCTOR OF PHILOSOPHY

Electrochromic nanostructures based on tungsten trioxide for reflective displays

MARIKA GUGOLE

Department of Chemistry and Chemical Engineering
CHALMERS UNIVERSITY OF TECHNOLOGY
Gothenburg, Sweden 2022

Electrochromic nanostructures based on tungsten trioxide for reflective displays
MARIKA GUGOLE
ISBN: 978-91-7905-737-4

Doktorsavhandlingar vid Chalmers tekniska högskola
Ny series nr 5203
ISSN 0346-718X

Department of Chemistry and Chemical Engineering
Chalmers University of Technology
SE-412 96 Gothenburg
Sweden

Cover: artistic representation of ions intercalating in Au-WO_3-Pt cavity.

Chalmers Digitaltryck
Gothenburg, Sweden 2022

Electrochromic nanostructures based on tungsten trioxide for reflective displays

MARIKA GUGOLE
Department of Chemistry and Chemical Engineering
Chalmers University of Technology

ABSTRACT

Our lives are dominated by the usage of displays. Every day we spend hours looking at displays and our eyes are surely affected by them. Reflective displays have gained a lot of attention in recent years due to their lower impact on our eyes' health, very low power consumption, and high performance in sunlight. In this work structural coloration and electrochromic materials have been explored to enhance the performance of this kind of display. We fabricated colored surfaces based on Fabry-Perót and plasmonic coloration. The nanostructures consist of a stack of three thin films in a metal-insulator-metal manner. By tuning the insulator thickness we can achieve red, green, and blue vibrant colors. Electrochromic materials, and in particular tungsten trioxide (WO_3), are implemented on top of the structures to act as on/off shutters. The optical properties of WO_3 can indeed be electrochemically tuned so that the reflectivity of the colored structures can be controlled with high contrast. Moreover, we have fabricated a similar kind of structural color, where WO_3 replaces the insulator middle layer in the cavity. In this configuration, the cavity is not shut on and off, but its resonance (the color seen) is shifted when WO_3 changes its optical properties. Hence, the surfaces can display several colors and a combination of two of them could generate all the colors necessary for a display. Finally, we have made a step forward towards a functioning display by succeeding in the fabrication, using several lithography steps, of the colored structures on thin film transistor (TFT) arrays.

Keywords: electrochromism, reflective displays, structural colors, WO_3.

List of publications

This thesis is based on the work contained in the following papers, referred to by Roman numerals in the text:

I **High-contrast switching of plasmonic structural colors: inorganic versus organic electrochromism.**
Marika Gugole, Oliver Olsson, Kunli Xiong, Jolie C. Blake, José Montero Amenedo, Ilknur Bayrak Pehlivan, Gunnar A. Niklasson, and Andreas Dahlin.
ACS Photonics 7.7 (2020): 1762-1772

II **Electrochromic Inorganic Nanostructures with High Chromaticity and Superior Brightness.**
Marika Gugole, Oliver Olsson, Stefano Rossi, Magnus P. Jonsson, and Andreas Dahlin.
Nano Letters 21.10 (2021): 4343-4350

III **Comparison of Electrodeposited and Sputtered Tungsten Trioxide Films for Inorganic Electrochromic Nanostructures.**
Marika Gugole, Oliver Olsson, Vandna Gupta, Romain Bordes, Anna Martinelli and Andreas Dahlin.
Submitted to ACS Applied Optical Materials

IV **Enhanced Electrochromic Switching Contrast in the Blue by 3,4-propylenedioxypyrrole - Implementation on Structural Colors**
Oliver Olsson, Marika Gugole, and Andreas Dahlin.
Submitted to Nanophotonics

Contribution to the listed publications

I First author (shared authorship with Oliver Olsson). Simulation of the RGB metasurfaces via Fresnel modeling, using MATLAB. Fabrication of the Fabry-Perót cavities and their characterization in terms of their reflectivity and color gamut. Simulation, deposition, and optical (reflection and ellipsometry) characterization of WO_3. SEM imaging of the nanoholes and dark field images of the striped samples. Contribution to the writing of the paper, particularly the experimental and the results section regarding WO_3.

II First author. Simulation of the Fabry-Perót cavities via Fresnel modeling, using MATLAB. Fabrication of the nanostructures and their characterization in terms of reflectivity and color gamut. Similarly, characterization of the commercial e-book and comparison with the presented surfaces. SEM and dark field images. Contribution to the writing of the paper, particularly the experimental and the results section.

III First author. Deposition of WO_3 via sputtering and electrochemistry. Characterization of the films in terms of their electrochromic properties (transmission) and their electrochemical activities (cyclic voltammetry). Fabrication of the Fabry-Perót cavities and their optical characterization in terms of reflectivity and color gamut. SEM image of the nanoholes array. Contribution to the FTIR measurements and interpretation of the results. Contribution to the writing of the paper, particularly the experimental and the results section.

IV Second author. Fabrication of the gold substrates and blue metasurfaces. SEM images of the cross-section of the metasurfaces.

List of abbreviations

ACH	Aluminum Chlorohydrate
AFM	Atomic Force Microscopy
APS	3-aminopropylsilatrane
CRT	Cathode Ray Tube
CIE	Commission Internationale de l'Éclairage
DC	Direct Current
FFS	Fringe-Field Switching
ICVT	Intervalence Charge Transfer
ITO	Indium Tin Oxide
In	Inorganic
IPS	In-Plane Switching
LED	Light Emitting Diode
LCD	Liquid Crystal Display
Or	Organic
OLED	Organic Light Emitting Diodes
PEDOT	Poly(ethylenedioxythiophene)
PET	Poly(ethylene terephthalate)
$pProDOTMe_2$	Poly(dimethylpropylenedioxythiophene)
pProDOP	Poly(propylenedioxypyrrole)
PS	Polystyrene
QCM	Quartz Crystal Microbalance
RF	Radio Frequency
RGB	Red, Green, Blue
SEM	Scanning Electron Microscopy
TFT	Thin Film Transistor
TN	Twisted Nematic
UV	Ultra Violet
VA	Vertical Alignment
XRD	X-Ray Diffraction

Contents

Chapter 1

Introduction

Since the appearance of the monochrome cathode-ray tube (CRT) in 1922 [1] displays have increasingly taken a huge part of our daily lives. Displays of all sizes are used for both work and recreation, ranging from giant displays in movie theaters to small screens on smartphones. The heavy usage of light-emitting devices has, however, affected our health. Dry eyes are accepted to be a consequence of digital displays usage [2], blue-light can affect our sleep and induce photoreceptor damage [3] without mentioning the high power consumption that some of these devices have [4].
"Emissive displays" refer to screens that emit light, which is what most of us are familiar with. Nonetheless, there is a type of display that does not emit light and it is known as a "reflective display". Like paper, reflective displays show images by reflecting ambient light. For this reason, they are often referred to as electronic paper. Popular examples of these displays are the Amazon Kindle™ series of e-book readers and the reMarkable™ writing tablet. There are several factors that can affect our eyes' health, such as the size of the screen or the surrounding environment [2]; reflective displays, however, appear to be less harmful to our eyes overall [5]. Despite this, there are a few reasons why these kinds of displays are not as popular as one might expect. For commercially available devices, the updating speed is slow, there is a need for a front light in a dark environment, and the depth of color is limited [6]. The focus of this work will be addressing the latter.
The fact that reflective displays do not have their own light source, but have to rely on the use of ambient light, puts very high demands on the reflectivity of the pixels. In the Amazon Kindle™ series, for example, images are formed by moving black and white particles with opposite charges inside the pixel. On top of that, red, green, and blue filters allow the display of

colorful images [7]. Consequently, the subdivision in three primary color pixels (which reduces the effective reflected light to 33% for each color), and the implementation of color filters, dramatically lowers the overall effective reflectivity [1].

1.1 Goals of this thesis

The results of the work presented in this thesis are an attempt to satisfy the need for higher reflectivity in reflective displays. In our research, we developed highly reflective red, green, and blue surfaces integrated with electrochromic materials for dynamic switching in a three-pixel design (Paper I). This combination maintains the high reflectivity and shows good contrast, i.e. the difference between the on and off states of a pixel, compared to commercially available devices. A different approach is also explored, where the subdivision of the pixel is replaced by a dynamic dual-pixel design (Paper II). This design not only shows superior brightness but also high chromaticity, i.e. quality of the color. Additional materials have also been studied and characterized with the aim of enhancing the reflectivity, quality, and speed of both designs (Paper III, Paper IV). We conclude by discussing the implementation of these structures for a future device.

1.2 Display technologies

This section will go through the different basic display technologies. Subsection 1.2.1 introduces the concept of emissive displays, which includes the most used and known types of displays on the market, such as liquid crystal displays (LCD), light emitting diodes (LED) displays, and organic light emitting diodes (OLED) displays. LCD are usually considered non-emissive since the core liquid crystal cell is non-emissive, however, they need some sort of back-light source. This essentially means that they emit light. However, LCD could also be reflective, if the ambient light is reflected from a surface placed behind the liquid crystal cell. The first type of LCD will be discussed under “emissive” and the second under “reflective”.

1.2.1 Emissive displays

In this section, we will briefly review the types of emissive displays that are, or were, popular on the market. The starting point is the CRT display, the first kind of display that was marketed for television screens [8]. This

display works by heating a cathode, which emits electrons. These electrons are accelerated by a voltage and deflected by an electromagnetic field. They eventually hit a screen that contains phosphors. Phosphors are substances that exhibit phosphorescence which means that they will glow when hit by an electron beam. The CRT update of images is done via raster addressing. This means that the electron beam rapidly scans through all the pixels in the front panel. Colored CRT displays can also be achieved with various techniques [9]. As far as television screens are concerned, CRT displays are out of the market for obvious reasons: size [10] and weight, particularly considering that a larger screen size requires a thicker body. The flat plasma display panel followed the CRT in the direction of flat displays. A matrix of fluorescent cells is used in this technology [11]. These cells are small fluorescent lamps where a plasma of inert gases is present, which generates UV light. The emitted light is then converted to visible light by impinging on the phosphors on the front panel of the cells [12]. There are three types of phosphors, one for each of the three primary colors (red, green, and blue). These types of displays could be made significantly larger than CRT displays and flat [13], however they suffered from high manufacturing costs [12]. During the same period (1960-1970), LCDs were also starting to emerge and hit the market [14]. As a rule, LCDs are usually made of two components, a liquid crystal panel, which we will describe shortly, and a back-light unit, since liquid crystal molecules do not emit any light. Originally, this back-light was composed of cold cathode fluorescent lamps, which were later replaced by light-emitting diodes (LEDs) [15]. Nowadays, LED is used to refer to displays incorporating liquid crystal display panels with LED back-lighting. Liquid crystals consist of anisometric (usually rod-like) molecules that form an orientationally ordered, and therefore also optically anisotropic, fluid. The fluidity and anisotropy allow for easy manipulation of the orientation direction and birefringence by means of electric fields. When placed between crossed polarizers, the electrically controlled liquid crystal thin film gives rise to amplitude modulation of light [16]. There are several configurations for liquid crystal displays, which can be seen in Figure 1.1 [14]: twisted nematic (TN), vertical alignment (VA), in-plane switching (IPS) and fringe-field switching (FFS). The principle is that back-light enters the liquid crystal cell through a polarizer, and passes through the liquid crystal layer which is a few micrometers thick. There, the state of polarization is altered depending on the local orientation of the liquid crystal. Eventually, it hits a second polarizer, which is orthogonal to the first polarizer. A picture is created by individually controlling the liquid crystal orientation in each pixel.

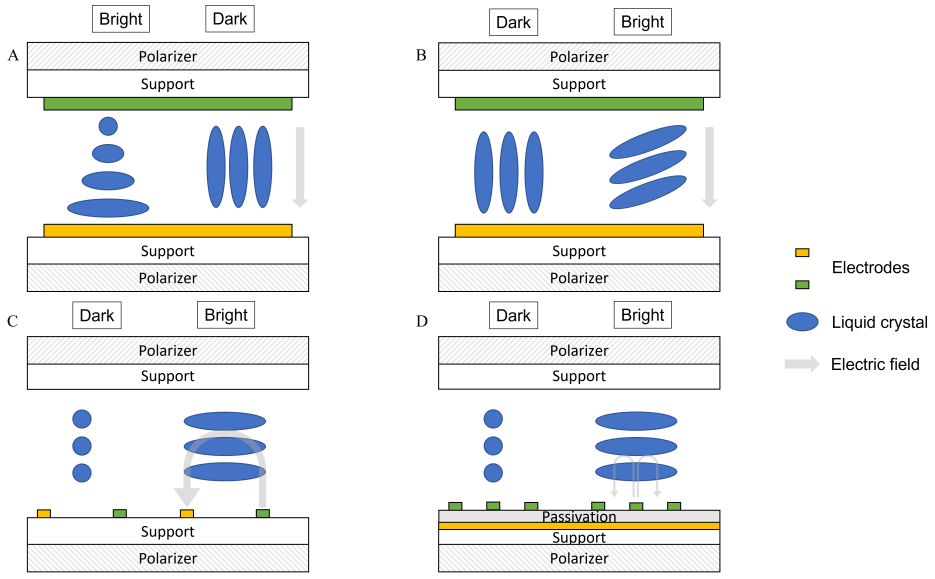

Figure 1.1: 4 configurations for liquid crystal displays in bright and dark state. The back-light is not depicted. A) Twisted Nematic, B) Vertical Alignment, C) In-Plane Switching, D) Fringe-Field Switching.

In the TN configuration (Figure 1.1 A), the liquid crystal's director (the local average direction of the molecules) forms a 90° twist between the supports. With no electric field applied the light follows the twist and escapes through the second polarizer. When a sufficiently strong electric field is applied the twist is "broken", the state of polarization is not changed and hence the light will not pass through the second polarizer. In the VA configuration (Figure 1.1 B), when no electric field is applied, the director is aligned vertically and the light is not transmitted, while it is transmitted when an electric field is applied. The IPS (Figure 1.1 C) and FFS (Figure 1.1 D) are similar configurations, where the director is rotated in-plane instead of vertical to horizontal. When the electric field is off, no light can be transmitted, while when the field is on the pixel is in bright state. The difference between these last two configurations is only based on the position of the electrodes, whose consequences are out of the scope of the thesis. However, one notable difference between the TN, VA modes and IPS, FFS modes is that the first two, due to the vertical sensitivity of the liquid crystal, are not suitable for touch screens as the alignment would be deformed when touching the dis-

play. This would heavily distort the transmitted intensity. There is no such problem with IPS and FFS designs [14].
Lastly, another important and competitive technology: OLEDs. The basic structure of OLEDs is fairly simple. It is a stack made of a metal reflector (cathode), an organic layer and a transparent conductor (anode) deposited on a substrate, as shown in Figure 1.2. A voltage is applied between the cathode and the anode and a current flows through the organic layer, which emits light via electroluminescence. Different organic materials are used to emit different colored light.

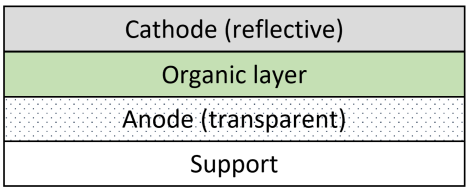

Figure 1.2: OLED structure.

1.2.2 Reflective displays

A reflective display is a type of display that does not emit any light of its own. Contrary to the most known and used displays in everyday life, like LED displays introduced above, reflective displays in their most fundamental form, do not include any light source, but only rely on the reflection of the ambient light [1], as shown in Figure 1.3. For this reason, they are also called electronic paper. For clarification, we underline that they do not possess any light source in their fundamental form, however, many commercially available reflective displays are equipped with a light source such as light-emitting diodes to enhance visibility in poor ambient light conditions [17]. The reflective display technologies that we will cover are electrophoretic, electrowetting, electrofluidic, electrochromic, and reflective LCD [18, 19, 6, 20].
In an electrophoretic display (Figure 1.4), black and white particles with opposite charges can be moved up and down with an electric field to regulate the amount of reflected light. The particles are placed in microcapsules between two electrodes. When the white particles face the top electrode, the pixel is white and when the black particles face the front electrode the pixel is dark. Greyscale is possible and color displays are achieved using color

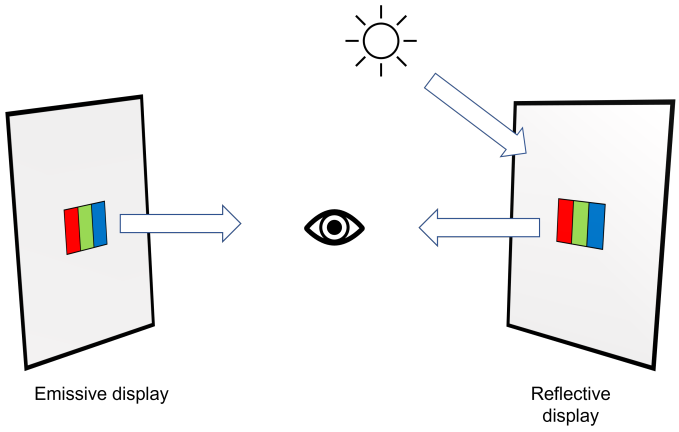

Figure 1.3: Emissive display vs reflective display.

filters on top of the capsules or particles with different colors. However, video speed is not possible.
In electrowetting displays (Figure 1.5 A), the on and off states of the pixels are controlled by changing the wettability of a surface by a potential. The surface is covered by a layer of water and a colored oil and by applying a voltage, it switches between being hydrophobic-oleophilic (no voltage) to hydrophilic-oleophobic (voltage) [21]. When the surface is hydrophobic, the colored oil forms a layer over the surface. When the surface becomes hydrophilic, the oil is pushed aside and no color is seen. However, the oil will still cover around 20% of the pixel area [19]. For this reason, a variant of the electrowetting display, called electrofluidic display (Figure 1.5 B), was introduced [22]. The electrofluidic technology is still based on electrowetting properties, although different in working principle and more complicated in design. The colored pigments are dissolved in water, and the structure is made of two parallel hydrophobic plates where an oil resides. There is a so-called reservoir where the colored water is hidden when no voltage is applied. When a voltage is applied and the plates become hydrophilic, the colored water is pushed out of the reservoir revealing the color while the oil is pushed through a duct.

Electrochromic based reflective displays (Figure 1.5 C), on the other hand, are much simpler in design [23]. Their pixels are usually comprised of two electrodes, an electrolyte, and one or two electrochemically active material layers. These structures are used for monochromatic displays, where

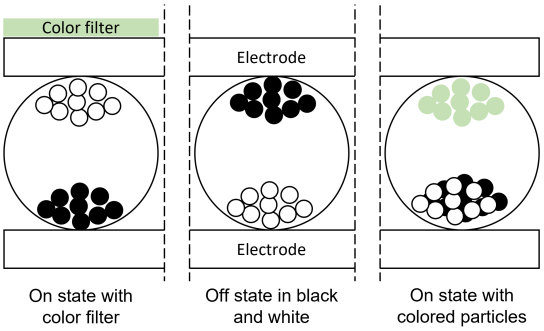

Figure 1.4: Schematic of different pixels' designs in electrophoretic displays. From left to right, on state using black and white particles and a color filter, off state using only black and white particles, and on state using different colored particles.

the pixel is set on and off by a potential that reduces and oxidizes the electrochromic material.
Finally, we have cholesteric liquid crystal displays (Figure 1.5 D), a type of LCD used in reflective mode [24]. Cholesteric liquid crystals are nematic crystals that spontaneously twist and form periodic, helical structures. As a result, they reflect light in a specific wavelength band depending on the pitch of the helix (a form of Bragg reflection in the visible). In cholesteric displays, the cholesteric liquid crystal is placed in front of a black surface and in between two electrodes. When no voltage is applied, the helix is normal to the substrate and the specific color is reflected. When a voltage is applied and the alignment is broken, there is no reflection and so only the underlying black surface is seen.

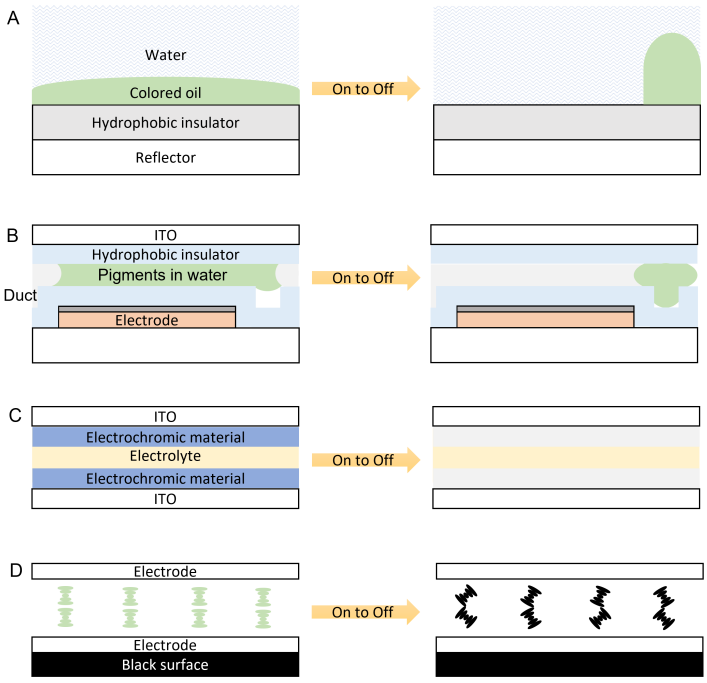

Figure 1.5: Schematic of A) electrowetting display, B) electrofluidic display, C) electrochromic display and D) cholesteric LCD.

Chapter 2

Theoretical background

2.1 Color theory

In this section we cover two important concepts which are crucial for understanding the results presented further in the thesis:

- The eyes' spectral sensitivity
- Colorimetry

In subsection 2.1.1 we will briefly go through what a color is and how our eyes are able to see colors. In subsection 2.1.2 we will present we can represent colors in a "universal way" with focus on the color "spaces" used in the thesis.

2.1.1 How the eye perceives colors

What we call "color" is nothing more than electromagnetic radiation that is reflected or emitted towards our eyes from any object with wavelengths confined between 380 nm and 740 nm. This is referred to as the visible part of the electromagnetic spectrum. Formally, the visible spectrum is defined as "any optical radiation capable of causing a visual sensation directly" [25] and has no precise limits, however, we will stick to the confinement written above. Figure 2.1 shows the electromagnetic spectrum including shorter and longer wavelengths, spanning from gamma rays to radio waves, which are invisible to us.
The perception of some wavelengths is due to the presence of photoreceptors cells in the eyes and, currently, three types of photoreceptors are known [26]:

- photosensitive retinal ganglion cells
- rods
- cones

The photosensitive retinal ganglion cells are recently discovered neurons that transmit light information to brain centers for "non-image" visual functions [27]. They explain why humans and mice retain light-responsive behaviors when rods and cones are lost [28]. Although their discovery has been revolutionary, they are out of the scope of this thesis and will not be discussed further.
The rods and cones are receptors that mainly take part to "image" visual functions, meaning that they are the receptors that allow us to see what is in front of us. The rods enable perception in black, white, and gray, while the cones are responsible for detecting colors [26]. There are 3 types of cones, each sensitive to a different part of the visible spectrum:

- S cones are sensitive to short wavelengths
- M cones are sensitive to middle wavelengths
- L cones are sensitive to long wavelengths

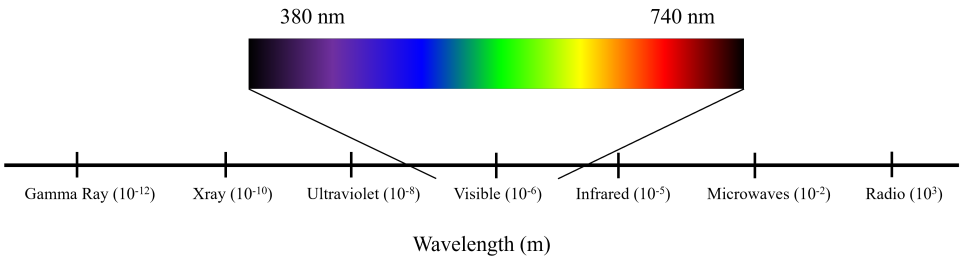

Figure 2.1: The electromagnetic spectrum, from gamma rays to radio waves with focus on the visible part between 380 nm and 740 nm.

In the following section we will see how colors can be represented in so-called color spaces which are based on the S, M and L cones sensitivity.

2.1.2 Color spaces

Having three cone types with different spectral sensitivities means that light can be represented by just three values: the three cone responses [29]. As a consequence, any color can be reproduced by mixing three primary colors, as long as their mix produces the same cones response. These colors are defined as primary in the sense that they are independent of each other: by mixing different amounts of the primary colors, all other colors can be obtained, but no primary color can be a mix of the other two primary colors. The amounts of each primary color required to obtain a non-primary color are called tristimulus values [30]. A color space is a 3-dimensional space that associates 3 coordinates to each color, each related to the corresponding tristimulus value.

During the 1920's Wright and Guild [31, 32] independently performed the so-called color matching experiments. They were experiments aiming at understanding the composition of light and reproducing it by using a mixture of 3 primary colors. In these experiments, observers were asked to recreate a test color by mixing 3 primary color light sources, red (R), green (G), and blue (B). The test color C would then be expressed by a sum of the primary color sources multiplied by their tristimulus coefficients, α, β, and γ, which represent the proportions of the red, green, and blue [33]:

$$C = \alpha R + \beta G + \gamma B \tag{2.1}$$

In both sets of experiments they used a reference white illuminant, the National Physics Laboratory Standard White Light. Guild, in his experiments, matched this white illuminant with a combination of the three sources and so determined how this reference white light was perceived by the human eyes. This led to the definition of the luminosity function $V(\lambda)$ (cf. Figure 2.2) which describes the sensitivity of the human eyes to the different wavelengths and peaks at around 555 nm. By multiplying the value of the luminosity function for each wavelength to the value of reflected light from any object at the respective wavelength, we can describe how human eyes will perceive the light coming from that object, and consequently its color (we will do this later in our results).
In 1931 the International Commission on Illumination (or CIE, for its French name) defined a CIE 1931 standard observer [34] by combining Wright and Guild data [35], which represents an average human eye response within 2 degrees angle [31]. The standard observer response was described with two sets of color matching functions showing the sensitivity of the 3 cones to the

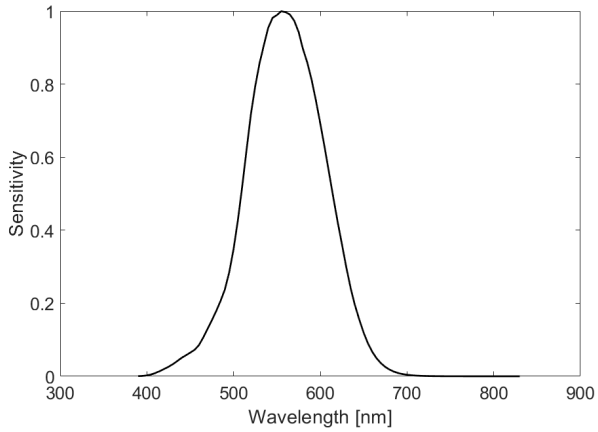

Figure 2.2: The luminosity function

primary colors, the CIE rgb and CIE xyz (here we refer to them as $x'y'z'$, to not create confusion with the xyz coordinates that will come later). Unfortunately, it seems impossible to find the original data of these functions, but they are still in use after modifications. Figure 2.1.2 shows the rgb color matching functions as modified by Stiles and Burch in 1955 (A) [36] and the $x'y'z'$ color matching functions as modified by Vos in 1978 (B) [37].

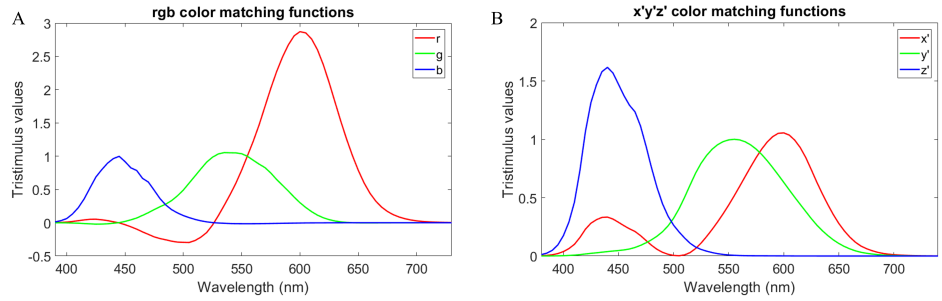

Figure 2.3: A) rgb color matching functions (Stiles and Burch, 1955). B) $x'y'z'$ color matching functions (Vos, 1978).

The RGB (similarly for XYZ) tristimulus values can then be calculated as following [30]:

$$R = \int_{380}^{740} r(\lambda)I(\lambda)dx \tag{2.2}$$

$$G = \int_{380}^{740} g(\lambda)I(\lambda)dx \tag{2.3}$$

$$B = \int_{380}^{740} b(\lambda)I(\lambda)dx \tag{2.4}$$

where $I(\lambda)$ is the spectral distribution of the light (power per unit areas that the source irradiates).

Although these are not the original 1931 CIE matching functions, it can still be noted that the rgb matching functions allow negative values. This means, in the color matching experiment, that the observer could not match the test color by any combination of the red, green, and blue sources. However, by adding the source to the test color instead, it could be possible to match the two lights. To better understand this, we briefly introduce how the experiments were conducted. One color, the test color, was projected and the participants were supposed to turn on, at an appropriate intensity, the red, green, and blue primary colors sources next to the test color until both were identical. For some colors, there was no combination that would match the test color. However, by moving the red source to the test color, hence projecting the test color plus an appropriate amount of red source, the two projected colors would match. Thus, some wavelengths have a negative value of r because the color was supposed to be subtracted, or /qadded negatively. The reason for the introduction of the $x'y'z'$ matching function was to avoid negative values of the coefficients, which were thought to be an easy source of error at a time when calculations were done manually. The $x'y'z'$ matching functions are then just a linear transformation of the rgb [38]. Moreover, the y' function now matches the luminosity function $V(\lambda)$. This is not accidental. Representing colors with 3 coordinates results a 3D plot which is not very convenient. The fact that the y' function matches the luminosity function allows the coordinates to be split. The Y coordinate represents the brightness of the object, since it is now an integral weighted with the luminosity function. While a transformation of the X and Y coordinates (x and y, Equations 2.5 and 2.6) [38], represent the color of the object. This is known as the xyY space and it will be used throughout this thesis.

$$x = \frac{X}{X + Y + Z} \tag{2.5}$$

$$y = \frac{Y}{X + Y + Z} \tag{2.6}$$

The x, y values are called chromaticity coordinates and are shown in the chromaticity plot, Figure 2.4, with the standard RGB coordinates as an example.

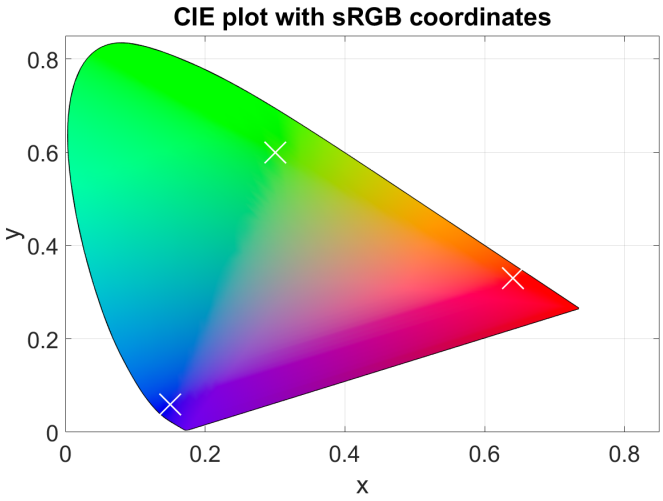

Figure 2.4: The chromaticity plot with standard RGB coordinates.

2.2 Electrochromism

In this section we will go through one of the core topics of the thesis: electrochromism and electrochromic materials. Subsection 2.2.1 is a brief introduction on what electrochromism is and which materials show this property. Subsection 2.2.2 will go more in detail through the electrochromic properties of oxygen deficient WO_3. This material is at the basis of all the results presented in the thesis and also one of the most studied and used electrochromic materials nowadays.

2.2.1 What is electrochromism?

Chromism is the property of some materials to exhibit a reversible color change in response to an external stimulus [39]. The stimulus can be temperature (thermochromism), light (photochromism), or an electric field (electrochromism). In this thesis, the focus will be on electrochromic materials. When applying a voltage between an electrochromic material and a counter electrode, both immersed in an electrolyte, a distributed electric field is set up and ions can intercalate and deintercalate in the film. The ionic species can then move in and out of the material and this results in a modulation of its optical properties [40]. Historically, electrochromic materials have been divided into subcategories according to their phase before and after the electrochemical reaction [41, 42]. Type I includes materials that are soluble and remain soluble during the whole electrochemical process. This category includes for example some viologens like aqueous methyl viologen which undergoes a reduction reaction and goes from a colorless state to an intense blue one. Type II includes materials that are soluble in their colorless form but become solid on the electrode surface after they undergo electron transfer. An example is cyanophenyl paraquat which is soluble and colorless before electron transfer and solid and olive green after the electrochemical reaction. Type III is the most interesting category for the scope of the thesis. It includes materials that always remain solid: most inorganic electrochromic materials like WO_3, NiO_2, and conductive polymers like poly(pyrrole), poly(thiophene), and poly(aniline).

2.2.2 Electrochromism in WO_3

While there are still questions about the mechanism behind the electrochromism in oxygen deficient WO_3, there are recurring theories that have been proposed in the literature. A discursive summary of these theories

is presented in this section. The first attempt to explain electrochromism in WO_3 was done by Deb in 1973 [43]. He explained the electrochromic properties of WO_3 by the F centers, or color centers, theory. Color centers are electrons bound to a negative ion vacancy [44], and in the case of WO_3, an oxygen vacancy. Color centers in WO_3 are formed via injection of an electron, either optically (photochromism) or electrically (electrochromism). The injected electron is then captured by the anion vacancy and becomes bounded to it. This electron can then be raised to an excited state via photon absorption. The core of the color centers theory is the fact that the injected electron gives rise to a localized state at the oxygen vacancy. However, this theory has been often ruled out because experiments show that the colored state of WO_3 corresponds to an increase of electrons localized at tungsten sites and not at oxygen vacancies [45]. This supports instead the intervalence charge transfer (ICVT) and polaron theories which are nowadays widely accepted [46] and sometimes considered equivalent [47, 48].

The ICVT theory was first proposed by Faughnan [49]. He claimed that WO_3 can form tungsten bronzes (compounds of tungsten trioxide and an alkali metal) of the type A_xWO_3 where the site A is occupied by an ion, like H^+ or Li^+. Upon intercalation, the ion is accompanied by an electron, which reduces the W neighbor site. In WO_3, the W sites are in the W^{6+} state thus turning into W^{5+} states. One W^{6+} and W^{5+} neighboring sites now have overlapping potential wells, so the electron in the W^{5+} can be excited by a photon to a state which overlaps with the neighbor site and subsequently fall into it. In summary, the core of the ICVT theory is the transfer of electrons externally injected to W^{6+} neighboring sites, which turn into W^{5+}, and the transfer of these electrons from the W^{5+} to a neighbor W^{6+} through photon absorption.

The polaron theory [47, 50, 51] is based on the same principle: the optical absorption rises from hopping between W^{6+} and W^{5+} neighboring sites. However, the injected electron is believed to enter a polaronic state [52]. The concept of polaron was first introduced by Landau in 1933 [53]. A polaron is a quasiparticle that describes the interaction between an electron and a lattice distortion. When ionic species are inserted, the accompanying electrons give rise to polaron states by changing the W valence state [54]. It is then possible for the polaron to hop between the newly formed W^{5+} state and neighbor W^{6+} state. However, both the ICVT and polaron theories fail to explain how oxygen vacancies play an important role and how an increase in oxygen vacancies correlates with an increase in color efficiency [46].

2.3 Structural coloration

In this thesis, we combine electrochromic materials with colored surfaces. These colored surfaces are not based on pigments or dyes, but on stacks of thin metallic and non-metallic films and rely on a phenomenon called structural coloration.

2.3.1 Principles of structural coloration

Structural coloration is a phenomenon widely seen in nature [55], for instance in the wings of butterflies and in the feathers of birds. The first explanation of structural coloration in nature, specifically about the structural colors of silverfish, dates back to Hooke in 1665 and Newton in 1730 [56]. Although a precise scientific definition of structural color is still to be settled [57], structural coloration is often presented in contrast to dyes and pigments. When we talk about the latter, we refer to molecules that interact with light, absorbing part of the incident light and reflecting another part. Essentially, absorption is the result of electrons in molecules interacting with the incident light, resulting in the elimination of part of the spectrum [57]. In contrast, structural coloration involves no exchange of energy between light and molecules. It is a consequence of the interaction between light and nano- and micro-structures such as thin-film interference, multilayer interference, diffraction grating, and photonic crystals [57]. Generally, colors arising from these phenomena are angle-dependent, meaning that the color seen varies with the angle of observation. These colors are defined as iridescent [58]. The structural colors presented further in the thesis are based on thin film interference, specifically Fabry-Perót cavities, and surface plasmons, which will be described in the following sections.

2.3.2 Single thin-film interference

Thin film interference from a single film is the most popular and yet simplest way of creating structural coloration [59]. Whenever light travels through a medium with a refractive index of n_1 and hits a thin film of another medium with a refractive index of n_2, it is both transmitted and reflected. The transmitted light then reflects from the bottom and transmits from the top of the second medium, interfering with the first reflected beam [60] (Figure 2.5). Based on the assumption that there is only one reflection at the first boundary and one at the second, we have only two beams interfering.
Suppose the source is monochromatic. The optical path length difference

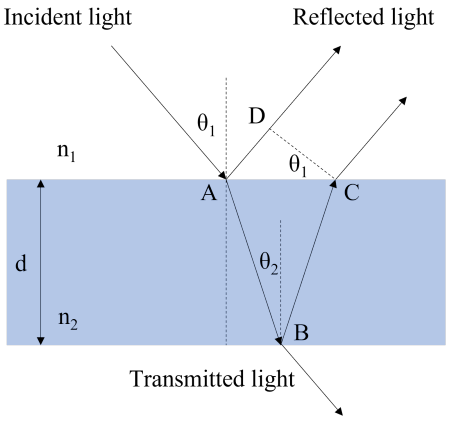

Figure 2.5: Schematic of light transmitted and reflected from a thin film.

between the beams in this case is

$$\Lambda = n_2 \times (\overline{AB} + \overline{BC}) - n_1 \times \overline{AD}$$

since $\overline{AB} = \overline{BC} = d/\cos(\theta_2)$ we can write

$$\Lambda = n_2 \times \frac{2d}{\cos(\theta_2)} - n_1 \times \overline{AD}$$

moreover $\overline{AD} = \overline{AC} \times \sin(\theta_1)$ and using Snell's law this can be written as $\overline{AD} = \overline{AC} \times \frac{n_2}{n_1} \times \sin(\theta_2)$, where $\overline{AC} = 2d \times \tan(\theta_2)$. Combining everything we find that

$$\begin{aligned}
\Lambda &= n_2 \times \frac{2d}{\cos(\theta_2)} - n_1 \times 2d \times \tan(\theta_2) \times \frac{n_2}{n_1} \times \sin(\theta_2) \\
&= n_2 \times \frac{2d}{\cos(\theta_2)} - 2d \times n_2 \times \frac{\sin^2(\theta_2)}{\cos(\theta_2)} \\
&= \frac{n_2 \times 2d}{\cos(\theta_2)} \times (1 - \sin^2(\theta_2))
\end{aligned}$$

and finally

$$\Lambda = n_2 \times 2d \times \cos(\theta_2) \tag{2.7}$$

At this point, we introduce the concept of constructive and destructive interference. Constructive interference occurs when the two interfering

waves are in phase, which means that their peaks and dips overlap. Destructive interference occurs when they don't overlap. In other words, if the path difference calculated in Equation 2.7 is an integer multiple of the wavelength, the two waves are in phase and we will have constructive interference; if it is a half integer multiple of the wavelength, the two waves will be out of phase, resulting in destructive interference. However, we also have to consider that the reflected light will experience a 180° phase shift if the second medium has a higher refractive index [57]. Hence, the conditions can be summarized as:

Constructive interference:

$$\Lambda = m\lambda \qquad (n_2 < n_1) \tag{2.8}$$

$$\Lambda = (m + 1/2)\lambda \qquad (n_2 > n_1) \tag{2.9}$$

Destructive interference:

$$\Lambda = (m + 1/2)\lambda \qquad (n_2 < n_1) \tag{2.10}$$

$$\Lambda = m\lambda \qquad (n_2 > n_1) \tag{2.11}$$

where m is an integer.

2.3.3 Multi-film interference

Multi-film interference can be seen as interference arising from a stack of pairs of thin films [57]. However, when considering multi-film interference, the total light reflected is the result of several transmissions and reflections of light at every interface. To deal with many layers, it is easier to introduce the Fresnel's coefficients. These coefficients have values between 0 and 1 and denote the fraction of transmitted and reflected light [61]. The coefficients for s-polarized light and p-polarized light are different, so there are 4 coefficients for each interface. It is easier to understand the multi-film system if we start from a single thin film (now using the Fresnel's coefficients) and consider the reflected and transmitted field amplitude first (those coefficients are indexed with small letters r and t) and just at the end convert it to intensity (those coefficients are denoted with capital letters R and T).

Looking at Figure 2.6, there are 3 different refractive indices n_1, n_2 and n_3, d_2 is the thickness of the film, E_0 is the electric field associated with the

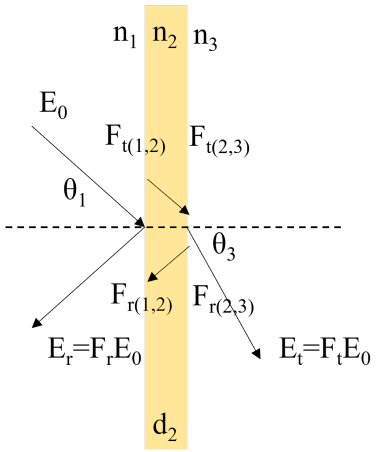

Figure 2.6: Schematic of single film interference with Fresnel's coefficients.

incident light, E_r is the electric field associated with the reflected light and E_t is the is the electric field associated with the transmitted light. θ_1 is the angle of incidence and θ_3 the angle of transmission. For each interface (i,j) we can calculate the Fresnel's coefficients as [61]:

$$F_{rs} = \frac{n_i \cos(\theta_i) - n_j \cos(\theta_j)}{n_i \cos(\theta_i) + n_j \cos(\theta_j)} \tag{2.12}$$

$$F_{rp} = \frac{n_i \cos(\theta_j) - n_j \cos(\theta_i)}{n_i \cos(\theta_j) + n_j \cos(\theta_i)} \tag{2.13}$$

$$F_{ts} = \frac{2n_i \cos(\theta_i)}{n_i \cos(\theta_i) + n_j \cos(\theta_j)} \tag{2.14}$$

$$F_{tp} = \frac{2n_i \cos(\theta_i)}{n_j \cos(\theta_i) + n_i \cos(\theta_j)} \tag{2.15}$$

Then, the coefficients that describe the effect of both the interfaces, but also the interference of the beams, are:

$$F_r = \frac{F_{r,12} + F_{r,23} e^{i2k_0 d_2 n_2 \cos(\theta_2)}}{1 + F_{r,12} F_{r,23} e^{i2k_0 d_2 n_2 \cos(\theta_2)}} \tag{2.16}$$

$$F_t = \frac{F_{t,12} + F_{t,23} e^{ik_0 d_2 n_2 \cos(\theta_2)}}{1 + F_{r,12} F_{r,23} e^{i2k_0 d_2 n_2 \cos(\theta_2)}} \tag{2.17}$$

Where k_0 is the free space wave-vector at the wavelength of interest. Equation 2.16 and 2.17 are valid for both s and p polarization as long as the respective $F_{(r \text{ or } t),(s \text{ or } p),(i,j)}$ are used.

To express these coefficients for the intensities, we can use:

$$F_R = \mid F_r \mid^2 \tag{2.18}$$

$$F_T = \frac{\mathrm{Re}(n_2 \cos(\theta_2))}{\mathrm{Re}(n_1 \cos(\theta_1))} \mid F_t \mid^2 \tag{2.19}$$

If we now consider a multi-layer system, we will have m materials, m-1 interfaces and m-2 layers, as shown in Figure 2.7.

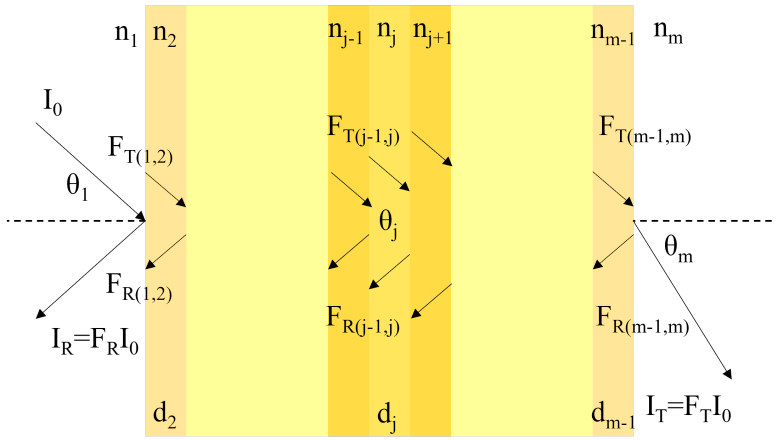

Figure 2.7: Schematic of multi-film interference.

In general, when passing from one material to another, each new angle can be expressed as follows::

$$\theta_{(j+1)} = \mathrm{Re}(\arcsin(\frac{n_j}{n_{(j+1)}}\sin(\theta_j)) - i \mid \mathrm{Im}(\arcsin(\frac{n_j}{n_{(j+1)}}\sin(\theta_j))) \mid \tag{2.20}$$

and the general expression of Equations 2.16 and 2.17 for a multi-layer system is expressed in terms of the so-called transfer matrix:

$$\Phi = \prod_{j=2}^{m-1} (\frac{1}{F_{t,[j-1]j}} \begin{bmatrix} 1 & F_{r,[j-1]j} \\ F_{r,[j-1]j} & 1 \end{bmatrix} \times \begin{bmatrix} e^{-ik_0 d_j n_j \cos(\theta_j)} & 0 \\ 0 & e^{ik_0 d_j n_j \cos(\theta_j)} \end{bmatrix}) \times \frac{1}{F_{t,[m-1]m}} \begin{bmatrix} 1 & F_{r,[m-1]m} \\ F_{r,[m-1]m} & 1 \end{bmatrix} \tag{2.21}$$

and finally

$$F_r = \frac{\Phi(2,1)}{\Phi(1,1)} \tag{2.22}$$

$$F_t = \frac{1}{\Phi(1,1)} \tag{2.23}$$

Subsequently F_R and F_T can be calculated from Equations 2.18 and 2.19 considering θ_1 and θ_m. This is known as the transfer matrix method.

2.3.4 Fabry-Perót cavities

One special case of multi-film interference is Fabry-Perót cavities. This cavity is made up of two parallel films spaced by a distance d. If the distance can be changed, then it serves as a Fabry-Perót interferometer, if the distance d is fixed it is referred to as a Fabry-Perót cavity [60, 62]. This structure is usually made up of semi-transmissive mirrors and its resonant effect, which can be solved using the transfer matrix method presented above, is seen in transmission mode. Only specific wavelengths can be transmitted after interfering in the cavity. Later in the thesis, we will present structural colors based on Fabry-Perót cavities, however, these structural colors are meant to be used in reflective mode. Therefore, one of the two mirrors in the cavity is not semi-transmissive, but is a bulk metal with as high reflectivity as possible. The transfer matrix method can still be used for modeling these structures to determine which wavelengths, and therefore which colors, are reflected.

2.3.5 Plasmonic nanostructures

The purpose of this section is to introduce the concept of plasmons and how they can be used to further select the desired color that is reflected from the Fabry-Perót-based structures discussed above. Plasmons are a vast topic and for the purposes of this thesis it is not necessary to understand them in depth, thus only a brief and phenomenological description is given. The focus will be on the excitation of surface plasmons via grating, which occurs in the top semi-transparent gold film of the Fabry-Perót cavities, due to the presence of an array of nanoholes.

Similarly to photons as quanta of light and phonons as quanta of vibration, plasmons are quanta of plasma oscillation [63]. There are different types of plasmons: bulk plasmons, wire plasmons, particle plasmons, and surface plasmons [61]. Our focus is on surface plasmons, which occur at the

interface between dielectrics and conductors [64]. The solution of Maxwell's equations can be used to demonstrate that an electromagnetic wave, called surface plasmon polariton, can exist at the interface between a metal surface and a dielectric. It is possible to excite surface plasmon polaritons with light, but just shining light on a metal surface is not sufficient. This is because the momentum of the photons is never equal to the momentum of the surface plasmons. [61]. It follows that somehow we need to add extra momentum to the photons, which can be expressed as:

$$\mathrm{Re}(k_x) = k\sin(\theta) + \Delta k_x \tag{2.24}$$

where k is the wavevector of the incident wave, k_x is the surface plasmon's wavevector in the surface plane, θ is the angle of incidence and x is the direction of propagation as shown in Figure 2.8.

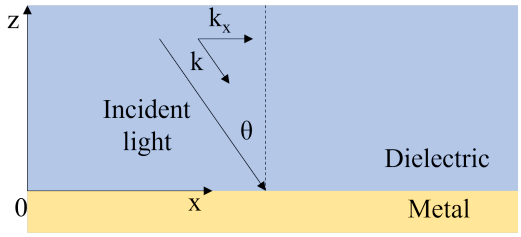

Figure 2.8: Light incident on a single metal film.

One way to excite surface plasmons and hence to satisfy Equation 2.24 is via grating excitation. If we call D the period of the nanoholes array, i.e. the spacing between each nanohole, (Figure 2.9) it can be shown that the x-component of the wavevector of the photon can be increased by multiples of $2\pi/D$. Hence the resonance condition can be expressed as [65, 66]:

$$\mathrm{Re}(k_x) = k\sin(\theta) + m\frac{2\pi}{D} \tag{2.25}$$

where m is an integer corresponding to the diffraction order of the grating. This means that by selecting the spacing between the nanoholes we can select the resonant wavelength that excites the surface plasmons, which will not contribute to the specular reflection.
In this work the incident light is always perpendicular to the surface, hence we only consider the case where $\theta = 0$.

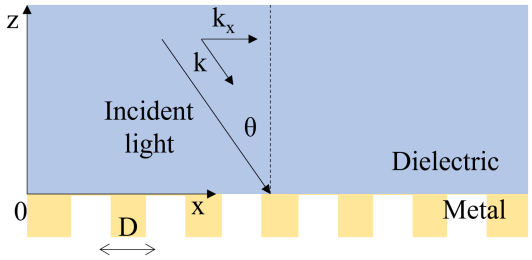

Figure 2.9: Light incident on a nanoholes array on a metal film.

2.4 Important parameters for reflective displays

In this section, we present some parameters that can be used to compare display technologies. In fact, defining meaningful universal parameters is difficult, especially when comparing emissive and reflective displays. Here, we discuss the parameters that will be used in the thesis and in the papers included in it.

Contrast

With contrast (C) we refer to the difference in reflectance (R) when a pixel is on or off, for a specific wavelength (λ) [7, 67]:

$$C(\lambda) = R_{\text{on}}(\lambda) - R_{\text{off}}(\lambda) \tag{2.26}$$

The contrast is wavelength-dependent as indicated in Equation 2.26, and this introduces some difficulties if this parameter is to be used for comparisons. If, for example, one wants to use an electrochromic material as a shutter, meaning that the electrochromic material switches between a transparent and black state and serves as on/off over a colored surface, one can consider the contrast for this material at the desired color wavelength. If one wants to know how good of a shutter it would be for a red pixel, one can consider the contrast at 630 nm, for green at 530 nm, and for blue at 470 nm. A color, however, is often associated with a wavelength band, rather than a single wavelength. Moreover, if one consider an electrochromic material that switches between a colored state and a transparent state used in a reflective display in black and white, as shown in the previous section, all the wavelengths become important to consider. It is, in fact, more meaningful to consider a contrast where the maximum and minimum reflection

are weighted with the luminosity function (V), as follows:

$$\overline{\Delta R} = \frac{\int_{380}^{740} V(\lambda)\Delta R(\lambda)\, d\lambda}{\int_{380}^{740} V(\lambda), d\lambda} \tag{2.27}$$

Using Equation 2.27, one considers the average reflection difference weighted with a function that accounts for the sensitivity of our eyes to different wavelengths, which is a more realistic representation of how our eyes would perceive the on and off states.

Switching time

The switching time (t_{switch}), as the name suggests, is the time needed for the material, or combination of materials, to switch from one state to another. Usually, the switching time does not consider the full switch, but the time needed to reach 90% or 95% of the full achievable contrast [7, 68]. In addition, it is usually defined in terms of the direction of the switch, such as from on to off or vice versa. This is because there can be a significant difference between these two times for some materials, especially electrochromic materials that rely on ion insertion and extraction to switch color. As an example, let us consider the contrast between the on and off states, C_{max}, and the time needed to reach 90% of the contrast, as shown in Figure 2.10.

$$t_{\text{switch}} = t_{90\%} - t_{\text{initial}} \tag{2.28}$$

Where t_{initial} is the time corresponding to the on state and $t_{90\%}$ is the time where the contrast is 90% of C_{max}.

Bistability time

As we have seen in many designs for reflective displays, one of the two states is often controlled by voltage. Eventually, once the voltage is turned off, the state will return to the previous state or to an intermediate state. With bistability time we refer to the time that a state is retained at open circuit. In the same way as the switching time, we measure the amount of time necessary to return to a certain percentage of the original reflectivity.

Power consumption

In comparing display technologies, power consumption is an important parameter, and for reflective displays it can be a selling point. In the previous

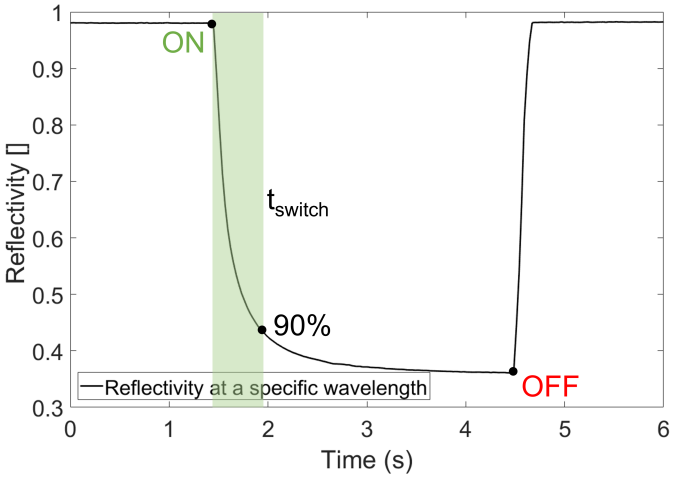

Figure 2.10: Switching time. State 1 is the transparent state, state 2 is the black state. The reflectivity is followed in time at a specific wavelength.

sections on emissive and reflective displays, one may have noticed that emissive displays generally require more power to operate [69]. This is especially true when the devices are used outdoors, where emissive displays must work against extremely bright ambient conditions. In this case, the power consumption can become significant. Reflective displays, on the other hand, will benefit from more light available for reflection. Therefore, power consumption is a crucial parameter, however it is difficult to define, especially since we do not work with completed devices. In this thesis power consumption will refer to the energy per area per switch [7].

Chapter 3

Experimental techniques

3.1 Electrochemical techniques

All electrochemical measurements are performed in the electrochemical cell, also called a three-electrodes setup. It is composed of an electrolyte, a counter electrode, a reference electrode, and a working electrode. As part of this thesis, the electrolyte is either propylene carbonate, in which lithium perchlorate is dissolved, or sulfuric acid. A platinum cage or coil serves as the counter electrode, with an active area much larger than the working electrode. The sample that is characterized, such as a conductive substrate on which tungsten oxide is deposited, is the working electrode. The reference electrode is a silver/silver chloride standard electrode (Ag/AgCl) or a silver/silver$^+$ electrode (Ag/Ag$^+$).

The potentiostat is the hardware that controls the electrochemical cell. It forces current through the counter electrode so that a voltage (E) is maintained between the reference and the working electrode. The current ($I(t)$) is the result of the measurement [70]. A schematic of the three-electrodes setup with the potentiostat is shown in Figure 3.1.
In terms of electrochemical techniques, we mainly used cyclic voltammetry and chronoamperometry. In both cases, one applies a potential between the working electrode and the reference electrode and records the current. However, in cyclic voltammetry one scans through a range of potentials at a determined speed, expressed in Volts/second, and often performs multiple scans. This technique is a powerful tool employed to investigate reduction and oxidation processes [71]. In this work, cyclic voltammetry was used to observe the reversible intercalation and extraction of ions in electrochromic materials. In chronoamperometry, a potential is applied immediately and

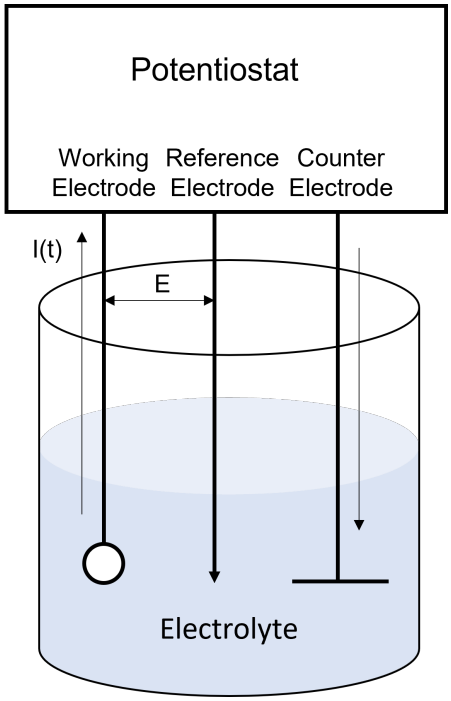

Figure 3.1: Schematic of an electrochemical cell connected to a potentiostat.

retained for a specified duration. The method is used to intercalate and extract ions from electrochromic materials while simultaneously studying their optical properties.

3.2 Thin film deposition

This section is a brief summary of the thin-films deposition techniques used in this work. In Subsection 3.2.1 electron beam evaporation is presented, in Subsection 3.2.2 radio frequency (RF) magnetron sputtering of WO_3 is described while Subsection 3.2.3 covers the electrodeposition of WO_3.

3.2.1 Electron beam evaporation

Electron beam evaporation is part of the physical vapor deposition techniques [72, 73]. In this category are all the thin films deposition techniques in which a source is evaporated and condensed onto a substrate. Figure 3.2

shows a schematic of a chamber for electron beam evaporation.

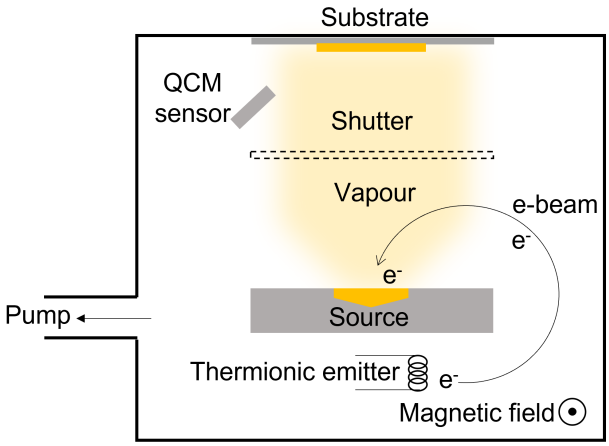

Figure 3.2: Schematic of a chamber for electron beam evaporation.

The process is done under vacuum (10^{-6} - 10^{-10} Torr) and the source is evaporated using an electron beam. The electron source is a thermionic emitter and the beam is bent using a magnetic field; this configuration is referred to as a 270° bent electron beam. The substrate holder and shutter are located above the source. Next to the substrate, a quartz crystal microbalance (QCM) sensor monitors the deposited thickness in real time.

3.2.2 RF magnetron sputtering of WO_3

Sputtering is also part of the physical vapor deposition techniques [72, 73]. There are different configurations and methods of sputtering and the one covered in this section is RF reactive magnetron sputtering. A schematic of a chamber for such a sputtering technique is shown in Figure 3.3.
The principle of sputtering relies on ion bombardment and momentum transfer from the plasma to the target. The substrate and target are the anode and cathode of a plasma discharge, respectively. The chamber is evacuated through a pumping line to a pressure of the order of 10^{-5} - 10^{-6} Torr. An inert gas such as argon and a reactive gas such as oxygen or nitrogen are let in the chamber. The power supply is a high RF voltage source of, most commonly, 0.5-1kV amplitude and a frequency of 13.56 MHz [72]. The ion from the target then reacts with the reactive gas before reaching the sample

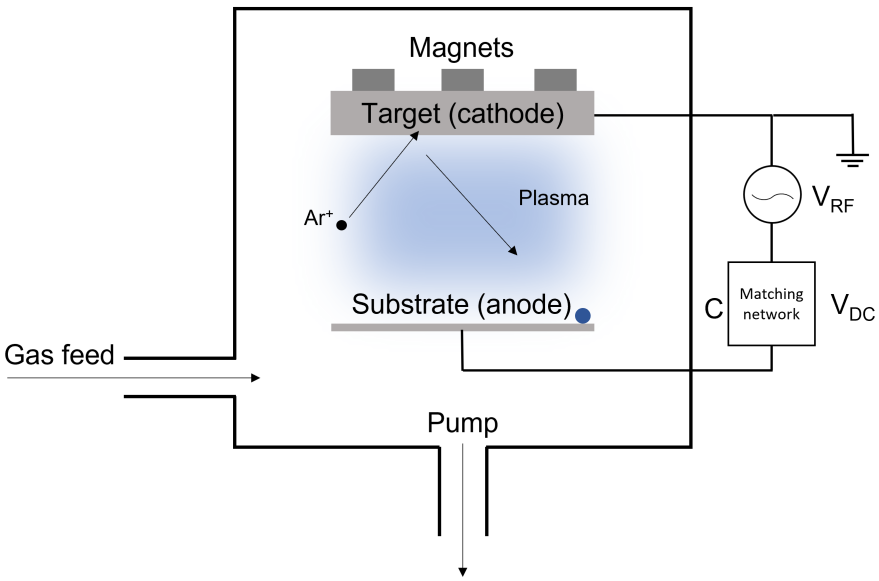

Figure 3.3: Schematic of a chamber for RF magnetron sputtering.

on the substrate table. A blocking capacitor and a matching network improve the power transfer to the plasma and develops the DC self-bias, which is a monitor of how much of the RF power is transferred to the plasma after losses [74]. The magnetron design is achieved by having magnets around the target to create a magnetic field that concentrates the plasma in its vicinity to enhance the ion bombardment of Ar ions on the target and consequently the sputtering rate.
In the case of RF reactive magnetron sputtering of WO_3 used in this work, the process could be optimized (contrary to electron beam evaporation which had pre-set recipes). The best-performing films, in terms of contrast, were fabricated using the following conditions:

- 32 sccm argon and 8 sccm oxygen
- 20 mTorr deposition pressure
- 150 W RF power

3.2.3 Electrodeposition of WO_3

The deposition solution was prepared by dissolving 1.03 g of $Na_2WO_4 \cdot 2H_2O$ in 250 ml of MilliQ water. Then the pH was lowered to 1.3 by adding 0.5 M of sulfuric acid. Lastly, 0.65 ml of H_2O_2 was added. The solution was placed on a magnetic stirrer overnight and was always prepared several days in advance. The electrochemical deposition of WO_3 was carried out in a three-electrodes setup, under continuous stirring, using platinum as the counter electrode and Ag/AgCl as the reference electrode. Two substrates were used: 20 nm gold on glass and 130 nm indium tin oxide (ITO) on glass. For both substrates, pulsed deposition was carried out. First, a 0.1 s pulse at -0.7 V, followed by a 0.1 s pulse at 0 V, and lastly a pause (open circuit) of 0.1 s. This was done for several cycles. The mechanism of electrodeposition can be described as follows [75]:

$$2WO_4^{2-} + 4H_2O_2 \rightarrow W_2O_{11}^{2-} + 2OH^- + 3H_2O$$

$$W_2O_{11}^{2-} + (2+3x)H^+ + 3xe^- \rightarrow 2H_xWO_3 + \frac{(2+x)}{2}H_2O + \frac{(8-x)}{4}O_2$$

$$H_xWO_3 \rightarrow WO_3 + xH^+ + xe^-$$

3.3 Lithography

In this section, the two types of lithography techniques used in this work are presented: colloidal lithography in Subsection 3.3.1 and laser lithography in Subsection 3.3.2.

3.3.1 Colloidal lithography

Colloidal lithography is a technique that takes advantage of the ability of nanoparticles to self-organize on surfaces, which makes them suitable as lithographic masks for the production of nano-sized surface features [76]. In this thesis, colloidal lithography was used to fabricate an array of nanoholes in gold and platinum thin films. Figure 3.4 shows a schematic of the colloidal lithography process where polystyrene (PS) particles are used as a mask.
First, the glass surface was treated with 50 W oxygen plasma for 30 s. This step makes the substrate hydrophilic. Then, a solution of 0.25 M aluminum chlorohydrate (ACH) was poured onto the substrate and let sit for 1 min. The excess solution was rinsed off with MilliQ water and the sample was dried with nitrogen. Subsequently, a 0.1% w/v solution of PS nanoparticles was poured and let sit for 2-4 minutes on the surface. If a higher density of

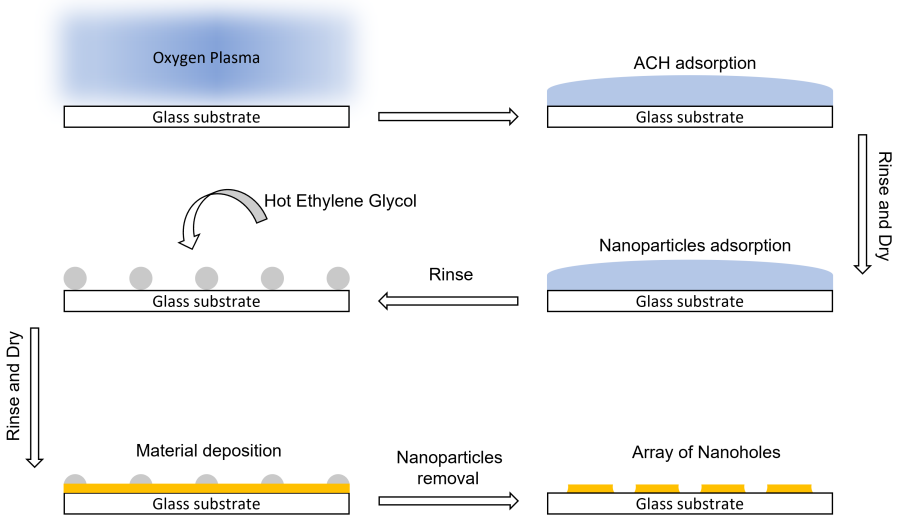

Figure 3.4: Schematic of colloidal lithography using polystyrene nanoparticles.

particles was required on the surface, sodium chloride was added to the solution [76]. The excess was then rinsed and hot ethylene glycol ($\sim 140°C$) was poured onto the substrate to partially melt the nanoparticles before a final MilliQ rinse and nitrogen dry. All the mentioned steps needed to be carried out while keeping the surface in a horizontal position and avoiding too much movement of the nanoparticles solution on the substrate. This was necessary to avoid a non-uniform distribution of the particles. When the self-assembled layer of PS nanoparticles was adsorbed, a material could be deposited onto them, with a maximum thickness equal to or slightly higher than the radius of the nanoparticles. After the deposition, the PS nanoparticles were removed using tape or rubbing, leaving an array of nanoholes behind.

3.3.2 Laser lithography

Laser lithography is part of the optical lithography techniques, in which light is used to expose a pattern onto a substrate with the assistance of

a light-sensitive material called photoresist [77]. This technique is used to expose special patterns onto a substrate before the deposition of another material, similarly to colloidal lithography discussed above. Before carrying out the laser writing, the substrate is cleaned and prepared for photoresist deposition, usually done by spin or spray coating. Once it is deposited, the photoresist is soft baked. This step removes the solvent in the photoresist and dries it. Now the substrate with photoresist is exposed to light: a laser scans all over the surface and writes on the photoresist. There are two types of photoresists, positive and negative, which react differently to light exposure. Positive photoresist becomes soluble when exposed to light while negative photoresist becomes insoluble. Figure 3.5 shows an example of a laser lithography process using a positive photoresist.

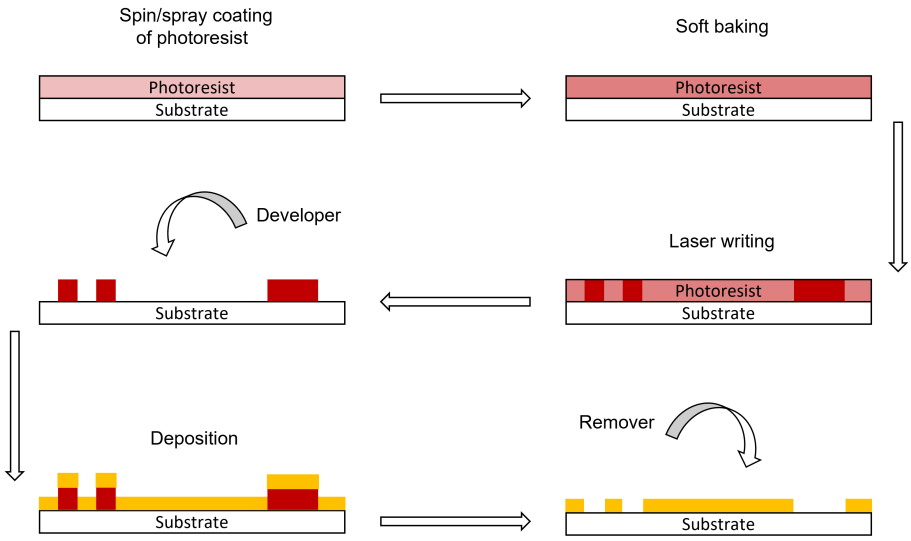

Figure 3.5: Schematic of a laser lithography process.

The last step before the material deposition is called development. The photoresist layer is now comprised of some soluble and some insoluble parts. During development, the developer, which can be an organic or aqueous-based solution, dissolves the soluble pattern, leaving behind exposed areas on which the material can be deposited. After the deposition, the leftover photoresist is removed. This can be done by soaking the sample in acetone

or an appropriate remover (this step is called lift-off).

3.4 Optical measurements

3.4.1 Reflection and Transmission

Optical reflection and transmission measurements were conducted with a home-built setup. The setup was comprised of a tungsten lamp connected to an optical fiber and several optical components such as focusing lenses, objectives, and a beam splitter. The setup was equipped with a lens that was used to focus the light beam onto the surface of the sample. The data was acquired by a spectrometer and the output was a reflection or transmission spectrum with the possibility of real-time display of the values for three different wavelengths of interest. For reflection measurements, a broadband dielectric mirror was used as the reference.

The setup could be used in combination with a specially designed cell which allowed to place the sample in a liquid. The cell could also serve as an electrochemical cell equipped with a standard reference electrode and a platinum coil as a counter electrode to perform optical and electrochemical characterization simultaneously. Analysis of the data was performed to determine the CIE coordinates and the corresponding color of the surfaces, both in liquid and in air. However, to determine the color of the metasurfaces in air, a colorimeter CM-700d from Konika Minolta was used.

3.4.2 Ellipsometry

Ellipsometry is a technique used to determine the optical constants and thickness of thin films [78]. It is based on the measurement of the change in polarization of light which is reflected from a surface. This change is expressed in terms of an amplitude ratio and a phase shift between s- and p- polarized light which is related, through the Fresnel equations, to the real and imaginary part of the refractive index of the studied material. The measurement is often done for different angles of incidence and different wavelengths (spectroscopic measurement). The setup required to perform ellipsometry measurements is rather simple. The light from a light source passes through a polarizer, reflects from the surface sample at a certain angle, and reaches an analyzer and a detector. However, this technique is an indirect technique. This means that the quantity that one measures, the polarization change, is not directly the interesting quantity and the

extraction of the desired data often requires complicated modeling skills especially for multilayers samples or unknown materials [77].

3.5 Other techniques

3.5.1 Profilometry

A profilometer is a simple instrument used to measure height profiles, roughness and shape of surfaces [77]. In a contact profilometer, a sharp stylus is in contact with the surface and it is moved across the sample, while its vertical position is recorded as a function of its position on the sample. The acquired data consist on the surface profile of the sample in the region of scanning. This techinque is easy and straightforward, however the measurement could result in damaging or contamination of the analyzed surface. Moreover, it requires hard samples to ensure an accurate and reproducible result.
The profilometer used in this work is a KLA Tencor Alpha-Step D-100 with a tip having 2.5 µm radius of curvature.

3.5.2 Scanning Electron Microscopy (SEM)

The scanning electron miscrocope is a type of microscope that utilizes a beam of electrons scanned over the sample surface to form an image [79]. The main component of the instrument are: the electron column, the specimen chamber and the pumping system. In the electron column the electron beam is generated by an electron gun. The beam then passes through a condenser, an objective lens, apertures, stigmators and scan coils to form a fine electron probe. In the speciment chamber an infrared camera allows the user to visualize the position of the substrate holder and different detectors can be present to collect backscattered and secondary electrons used to reconstruct the final image.

Chapter 4

Summary of results in papers

This chapter gives a brief summary of the results from Paper I, Paper II, Paper III, and Paper IV. More details are presented and discussed in the appended papers.

4.1 Plasmonic structural colors

In Paper I, we successfully fabricated plasmonic structural colors with high reflectivity and good chromaticity, electrochemically stable in organic solvents, referred to as metasurfaces. The structures' design was based upon previous publications [67, 80]: a combination of Fabry-Pérot modes and plasmonic effects. However, in this work, the material selection was constrained by the dissolution of the silver mirror in the electrolyte that we chose for the electrochemical characterization, lithium perchlorate in propylene carbonate. This electrolyte is non-volatile and suitable for device implementation. Hence, the silver mirror used previously was replaced with an aluminum mirror. Figure 4.1 A shows a schematic of the metasurfaces and the corresponding reflectivity spectra measured using a colorimeter with a collection angle of 8°, in air and under diffuse illumination to simulate ambient light. The metasurfaces were a stack comprised of an aluminum mirror (100 nm), an alumina spacer layer, and a top gold film (20 nm). The alumina spacer had a variable thickness, which determines the color of the metasurface by a change in the cavity resonance. Three thicknesses were selected that produced the three primary RGB colors: 61 nm, 110 nm, and 95 nm respectively. For the green and blue surfaces, an array of nanoholes was fabricated via colloidal lithography in the gold film using polystyrene nanoparticles with a diameter of 147 nm. The array of nanoholes introduced

a plasmonic activity in the red region which resulted in a suppression of the reflectivity in that region. For this reason, no nanoholes were fabricated on the red sample. A picture of the metasurfaces and an SEM picture of the array of nanoholes can be seen in Figure 4.1 B. Figure 4.1 C shows the 1931 CIE diagram for the three metasurfaces compared to the standard RGB gamut. Figure 4.1 D shows the dark field image of a metasurface comprised of red, green, and blue stripes ("white") which shows no scattering for the red stripe and orange-red scattering for the green and blue stripe, due to the presence of the array of nanoholes.

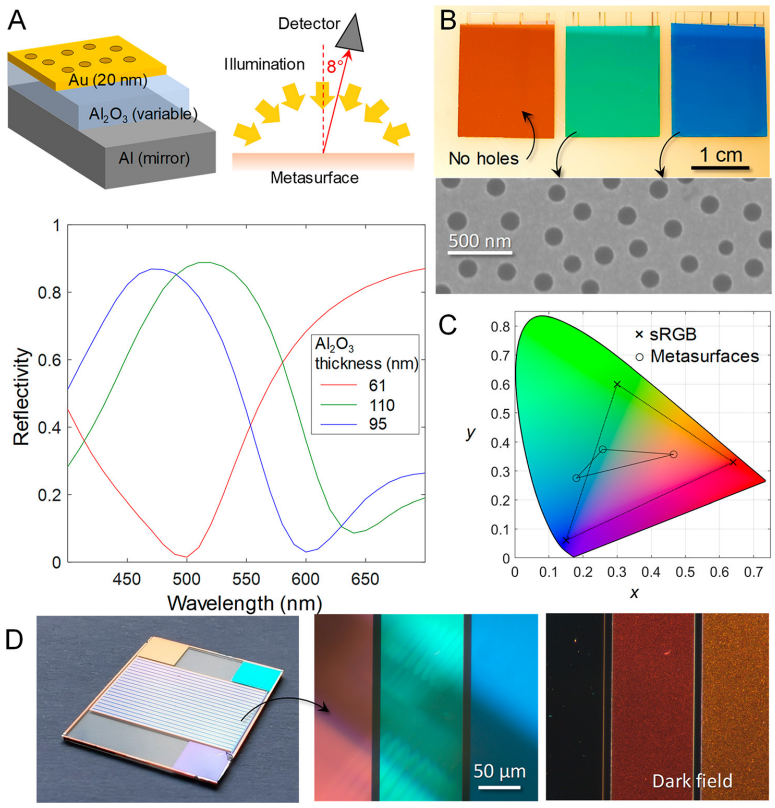

Figure 4.1: Plasmonic structural colors. (A) Schematic and reflectivity spectra of the RGB metasurfaces. (B) Photo of the metasurfaces and SEM image of the nanoholes array. (C) CIE chromaticity coordinates (circles) compared to the standard RGB gamut (crosses). (D) A "white" surface made by RGB stripes. Microscopy images showing the colors in bright and dark field illumination. Reproduced from Paper I.

4.2 Organic vs inorganic electrochromics

The optimal thicknesses for red, green, and blue metasurfaces were predicted differently for the organic and inorganic material (the work on the organic material was not carried out by the author of the thesis). The electrochromic polymer was first electropolymerized on a 20 nm gold surface from a 10 mM monomer solution in 0.1 M $LiClO_4$ in propylene carbonate using cyclic voltammetry between -1 V and +1.1 V (vs Ag/Ag^+, as for all potentials in Paper I) at 200 mV/s. The transmission difference between dark and bright states was measured at the wavelengths corresponding to red, green, and blue (470 nm, 530 nm, 630 nm) and 580 nm (maximum achievable contrast), for a different number of deposition cycles (different thicknesses). This is shown in Figure 4.2, where the dark and bright states correspond to an applied voltage of -1 V and +0.5 V in 1 M $LiClO_4$ in propylene carbonate respectively. From this data it was possible to determine the

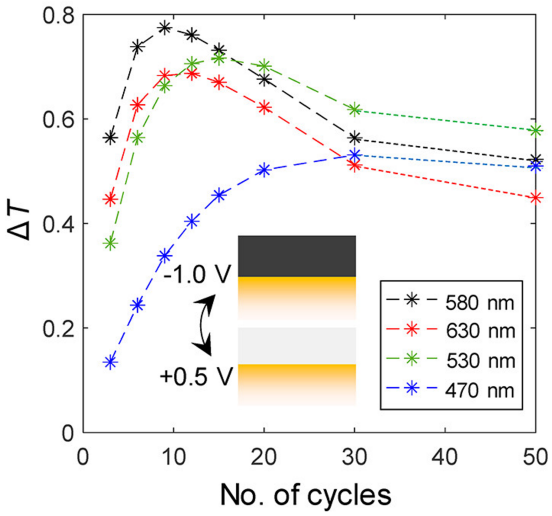

Figure 4.2: Contrast as ΔT for different thicknesses (cycle numbers) of the $pProDOTMe_2$ films at different wavelengths. The contribution from the extinction of the thin Au film has been removed. Adapted from Paper I.

thickness corresponding to the highest contrast for each color. The deposition on the metasurfaces was then carried out by first depositing a film whose thickness was close to the optimal thickness and then, while monitoring the contrast during deposition, continuing to polymerize until the

maximum contrast was achieved. The ideal values of thickness were 6, 9 and 15 cycles for red, green and blue respectively.

Due to interference effects, the selection of the thickness corresponding to the maximum contrast at the RGB wavelengths for the inorganic WO_3 was done using full Fresnel modeling. Figure 4.3 shows the Fresnel simulations of RGB metasurfaces immersed in the electrolyte (dashed) and with different WO_3 thicknesses (solid), excluding the nanoholes. From these simulations we could infer the thicknesses which would give the best contrast without affecting the color of the metasurfaces. The thicknesses were 130 nm, 180 nm and 130 nm for red, green, and blue respectively.

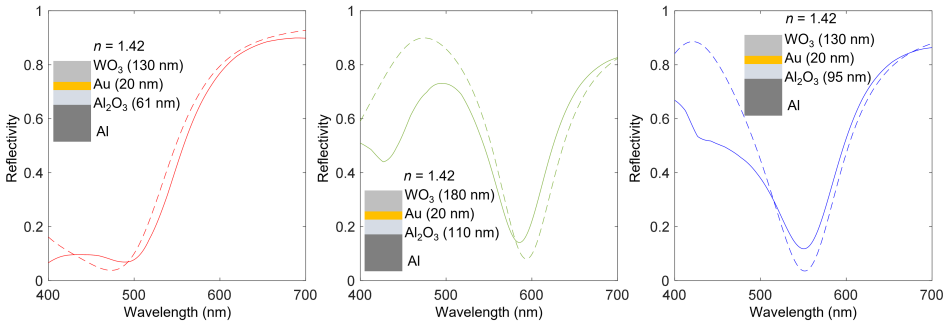

Figure 4.3: Simulations of RGB metasurfaces with WO_3 (solid) and without (dashed). Reproduced from Paper I, Supporting Information.

Figure 4.4 shows the result of the comparison between organic and inorganic electrochromisms in terms of contrast. The inorganic material showed the highest contrast for all colors, both when considering the absolute reflectivity (Figure 4.4 A) and the reflectivity difference weighted with the luminosity function (Figure 4.4 B).

The second parameter included in the comparison was the switching time (considering 90% of the contrast). To evaluate the switching time for both the organic and inorganic options we monitored the transmission at 470 nm, 530 nm, and 630 nm while applying the potentials corresponding to the on and off states. Both samples were simply 200 nm of electrochromic material on a 20 nm gold substrate. The organic film switched equally fast (less than about 1 s) in both directions, dark to bright and bright to dark, and with similar speed for all the wavelengths. The inorganic WO_3 switched much slower, around 10 s, from bright to dark. The switching time of the reverse switch was comparable with the one of the organic material. In terms of bisability,

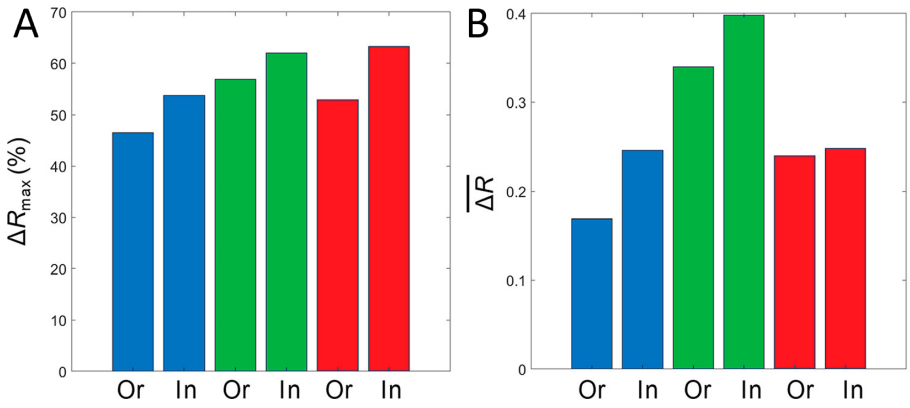

Figure 4.4: Contrast comparison of RGB metasurfaces with $pProDOTMe_2$ (Or) and (B) WO_3 (In) in terms of (A) absolute reflectivity and (B) reflectivity weighted with the luminosity function (Equation 2.27, between 340 nm and 780 nm). Adapted from Paper I.

both organic and inorganic material showed basically perfect bistability in the bright state, which is essentially the equilibrium state. For the dark state, the polymer and the metal oxide showed different bistabilities, with the polymer showing a dependency on the wavelengths. However, they both drifted very slowly. Lastly, we compared the electrochromic materials in terms of power consumption, one of the main motivations for electronic paper displays. We calculated the power consumption considering the energy per area per switch [67]. The results were 1-2 mJ/cm^2 for $pProDOTMe_2$ and 40 mJ/cm^2 for WO_3.

4.3 Structural colors based on electrochromics

In Paper II, we presented two designs for the metasurfaces, where the WO_3 replaces the aluminum oxide spacer layer [81, 82, 83]. This allows the pixel to show a broad range of colors since the electrochromic material makes the cavity resonance tunable (by changing the refractive index during ion intercalation). Consequently, the standard RGB subpixel configuration could be replaced by 2 pixels, which would improve significantly the performance of a reflective display. Moreover, in one design, the counter electrode and the electrolyte can be chosen for best electrochemical performance and long-term stability since they are placed behind the nanostructure.
Figure 4.5 A shows a schematic of the designs. On the left, we denote "conventional" the combination in which the transparent conductor and electrolyte are placed in front of the colored surface. In this case, an array of nanoholes was fabricated via colloidal lithography in the thin gold top film, to allow the ions to reach the middle electrochromic layer for intercalation and extraction. On the right, the "reverse" design is shown, in which the electrochemical components are placed behind the colored surface. Hence, the array of nanoholes was fabricated in the mirror, which was in contact with the electrolyte. The conventional structure is made of 50 nm platinum, variable WO_3 spacer layer, and 20 nm gold. The reverse cavity was instead comprised of the same gold film and variable WO_3, however, the platinum mirror was up to 70 nm. The colloids used to fabricate the nanoholes array were 147 nm in diameter. Figure 4.5 B shows one picture of 5 different samples for the conventional and one picture for the reversed design. On the right, it shows two pictures of how the samples looked from the platinum side. The two designs resulted in the same visual color for similar WO_3 thicknesses. Figure 4.5 C shows an SEM picture of the nanoholes in the gold film in the conventional design (top) and in the platinum in the reverse design (bottom).

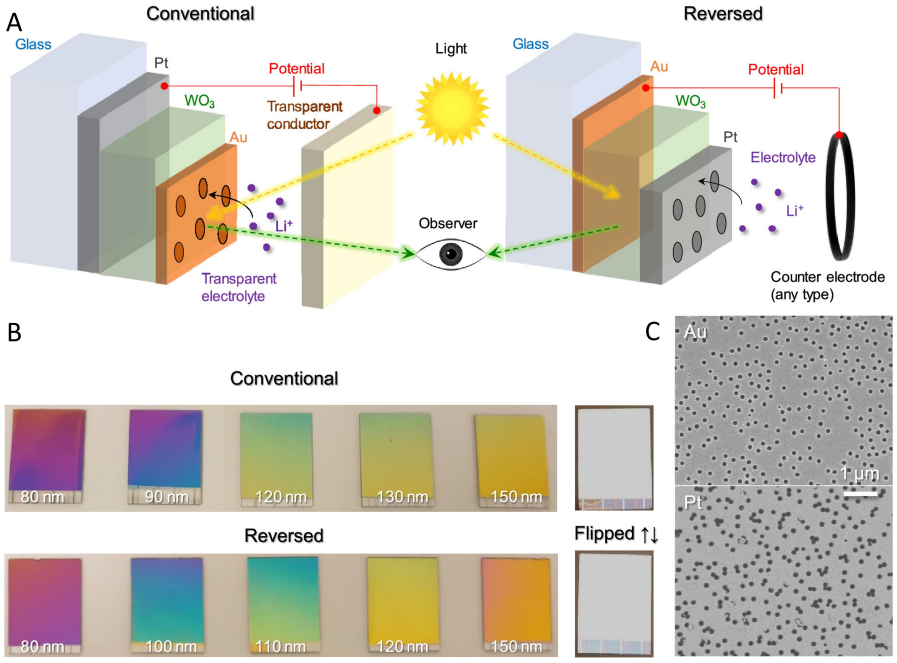

Figure 4.5: Conventional and reverse designs. (A) Schematics of the nanostructures. (B) Photos of the samples with different thicknesses of WO_3, front and back. (C) SEM images of nanoholes in gold and platinum. Reproduced from Paper II.

Different WO_3 thicknesses gave rise to different resonances of the cavity. This can be seen visually in Figure 4.5 B and in terms of reflectivity spectra in Figure 4.6. For the conventional design, the samples were im-

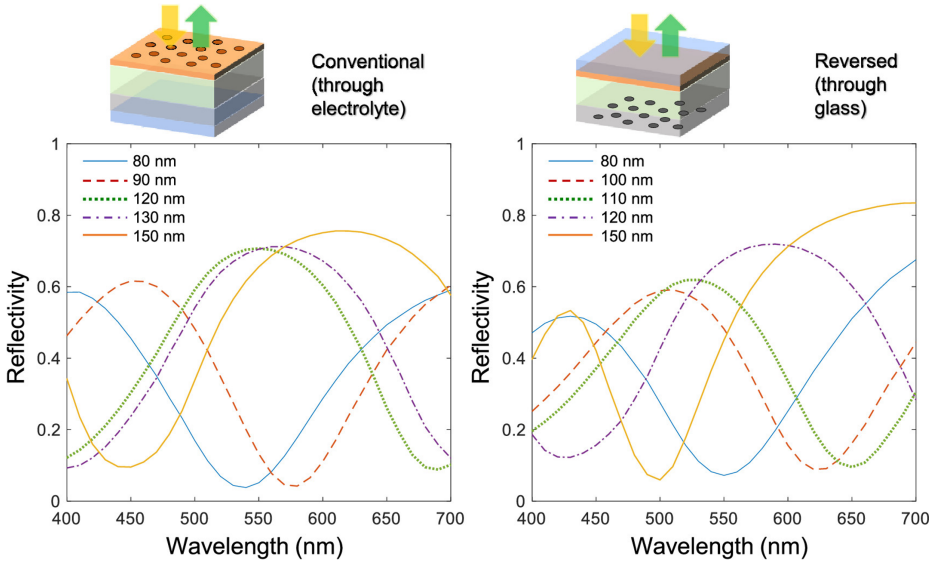

Figure 4.6: Absolute reflectance spectra measured under diffuse illumination for different WO_3 thicknesses. Adapted from Paper II.

mersed in a liquid with the same refractive index as propylene carbonate to simulate how the spectra would look when the metasurface is immersed in the electrolyte. The reverse design was instead measured in air, through the glass support. Several colors could be achieved by simply choosing the correct WO_3 thickness. Moreover, similar colors could be achieved for the same WO_3 thickness for both conventional and reverse design. However, in a device configuration, the reflectivity of the conventional design would not be retained. This is because a transparent conductor, such as ITO, and the electrolyte would be introduced in front of the colored surface to allow the electrochemical switch. We measured the losses that the electrochemical setup would introduce in a real device for the conventional design to underline the improvement in the reverse design, cf. Figure 4.7.
From this point, we will focus on the performances of the reverse design and in particular on the electrochemical tuning of the cavities. To do so, a potential was applied to the metasurfaces ($\pm$ 1.5 V vs Ag/Ag^+) while

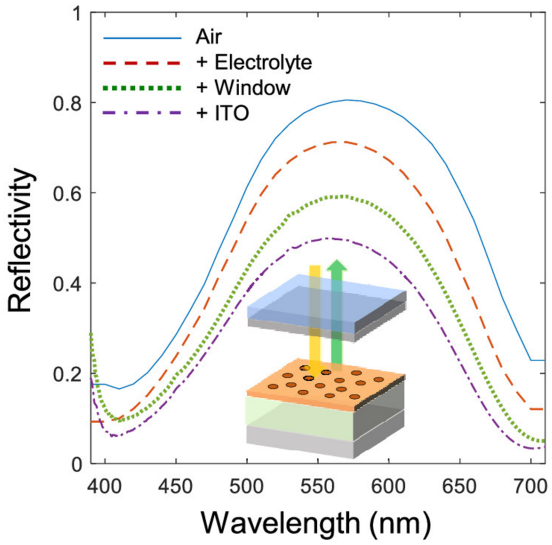

Figure 4.7: Reflectivity losses when electrolyte and counter electrode are introduced for the conventional design. Adapted from Paper II.

simultaneously monitoring the reflectance. As an example, the switching of a reverse cavity with 100 nm WO_3, in terms of reflectivity change, is shown in Figure 4.8 A (more spectra are reported in Paper II). The 3 states in the reflectivity spectra correspond to WO_3 being in bright, dark and one intermediate state. Of course, there are more intermediate states that can be achieved by simply interrupt the insertion of the ions at different times (i.e. applying a potential for different times). This can be seen in Figure 4.8 B which shows the CIE coordinates of 4 different reverse cavities with different WO_3 thicknesses. The black curves represent the CIE coordinates at several stages of the ion intercalation (bright, dark and several intermediate states). The numbers next to the switching curves represent the Y values at the bright and dark state. It is important to show the Y values because they are a representation of how human vision perceives color. It is not obvious that a surface with higher absolute reflectance would appear brighter than one with lower absolute reflectance since this depends on the different sensitivity of the eyes for different parts of the spectrum. This can be noticed for sample III, where the Y value increases when WO_3 is in dark state since the resonance of the cavity moves towards the green region of the spectrum.

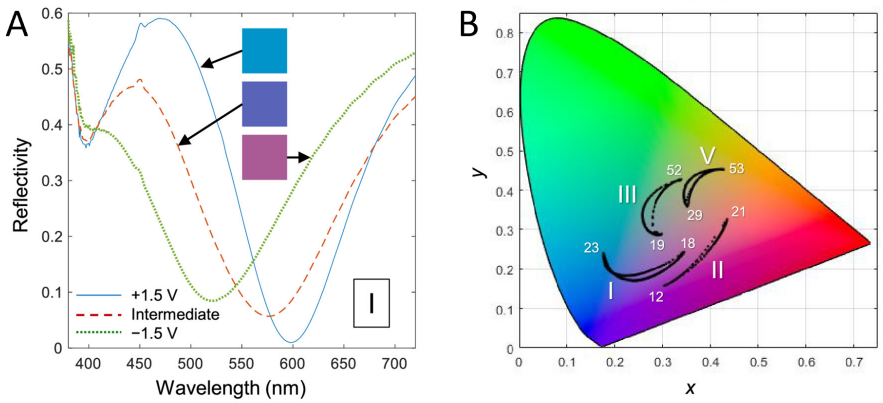

Figure 4.8: Electrochemical color tuning. A) Reflectivity spectra of a reverse cavity at different intercalation stages. B) CIE plot of 4 reverse cavities with Y value corresponding to bright and dark state of WO_3. Adapted from Paper II.

Lastly, we considered a combination of two reverse cavities and simulated their performance in a device configuration, which we compared with the latest e-reader in color on the market (PocketBook color). The pixels are considered to be made of 90 nm WO_3 (on 35% of the pixel) and 110 nm (on 55 %) with a remaining 10% considered as a 50% reflective surface. This assumes a fill factor of 0.9 which is reasonable in a device (see Figure 5.2). The CIE coordinates of several states corresponding to a dual pixel simulation using the reverse design are shown in Figure 4.9 A. With only 2 pixels it is possible to span over a broad range of colors. Moreover, it shows how our design could outperform the latest commercially available option whose gamut is represented by the black triangle.
As mentioned before, it is important to consider the Y values. This is illustrated in Figure 4.9 B. We considered a few examples of colors achievable with the dual pixel combination and compared them with the red, green, blue, black, and white pixels of the e-reader. All the combinations could outperform the e-reader.

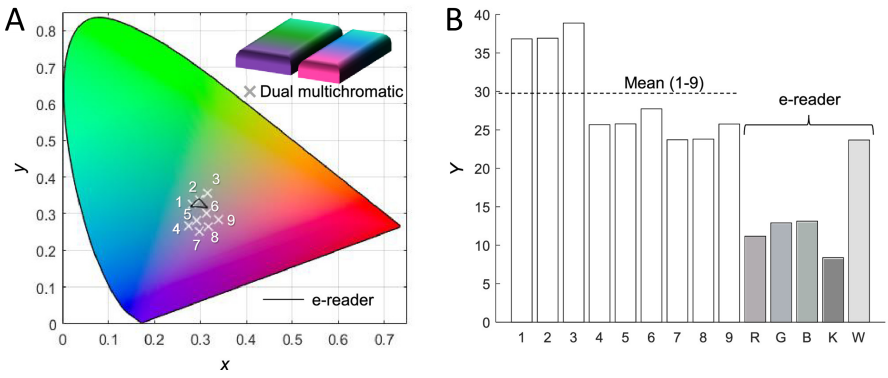

Figure 4.9: Simulation of a device with dual pixel configuration. A) CIE coordinates of a few selected colors achievable with the simulated device (white crosses), together with the gamut that can be shown in a commercial device (black triangle). B) Corresponding Y values. Adapted from Paper II.

4.4 Electrodeposited vs sputtered WO_3

In Paper III, we compared the performance of WO_3 deposited with sputtering (see subsection 3.2.2) and electrochemistry (see subsection 3.2.3). Sputtering is a well-established technique to fabricate the material [84], but in recent years a lot of attention has been given to its electrodeposition, which represents a facile and less expensive method to achieve very high optical modulation and switching speed [75].

Morphological characterization

We performed AFM measurements on electrodeposited and sputtered WO_3 films. The surface of the electrodeposited films (Figure 4.10 A) was very rough with an average roughness of 9.48 nm ± 1.18 nm. The surface of the sputtered one (Figure 4.10 B) was smooth and compact, with an average roughness of 1.80 nm ± 0.67 nm.

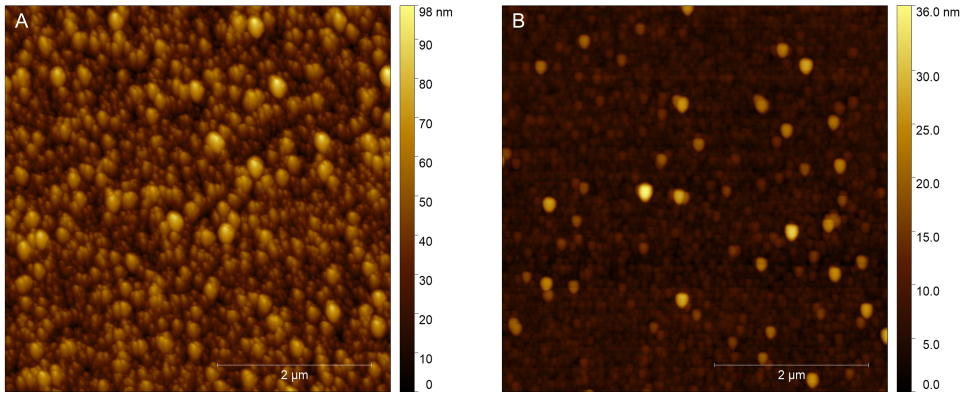

Figure 4.10: AFM (tapping mode) of A) electrodeposited and B) sputtered WO_3. Adapted from Paper III.

Optical characterization

The characterization was carried out in 2 different electrolytes: 0.5 M sulfuric acid and 1 M $LiClO_4$ in propylene carbonate. In both electrolytes the contrast increased with the thickness and eventually reached a plateau or stopped increasing significantly. In sulfuric acid this limit was reached for thinner films, about 200 nm, while for propylene carbonate thicker films were nedeed, about 300 nm. We attributed this to a difference in intercalation of lithium ions and protons due to their size. Despite this, in both eletrolytes a similar optical modulation could be reached, with sputtered films always performing slightly better (Figure 4.11 A). In Figure 4.11 B, the spectra in the dark and bright states for the thicknesses corresponding to the highest contrast are reported. The spectra show that both electrodeposited and sputtered films could reach ultra-high optical modulation in sulfuric acid of 98% in the red region, as previously reported for electrodeposited film by Cai et al. [75]. Sputtered films could, however, perform almost as good in propylene carbonate, showing a contrast of 93% in propylene carbonate, while electrodeposited films reached a contrast of 87%.

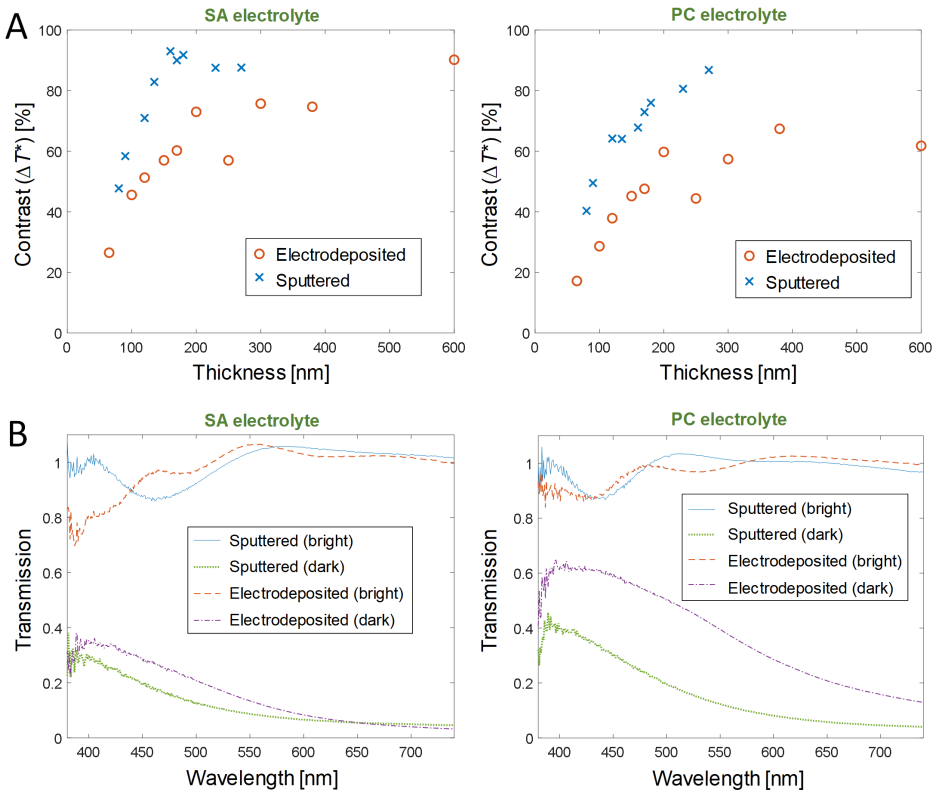

Figure 4.11: Average contrast vs thickness and highest achievable contrast. A) Average contrast achieved for different thicknesses of electrodeposited and sputtered WO_3 in sulfuric acid and propylene carbonate. B) Transmission spectra for the thickness which gave the highest contrast for electrodeposited and sputtered films in the two electrolytes. Reproduced from Paper III.

An important parameter to consider when comparing electrochromic films is the switching time. The switching time of electrodeposited and sputtered films of different thicknesses, in sulfuric acid and propylene carbonate is shown in Figure 4.12.

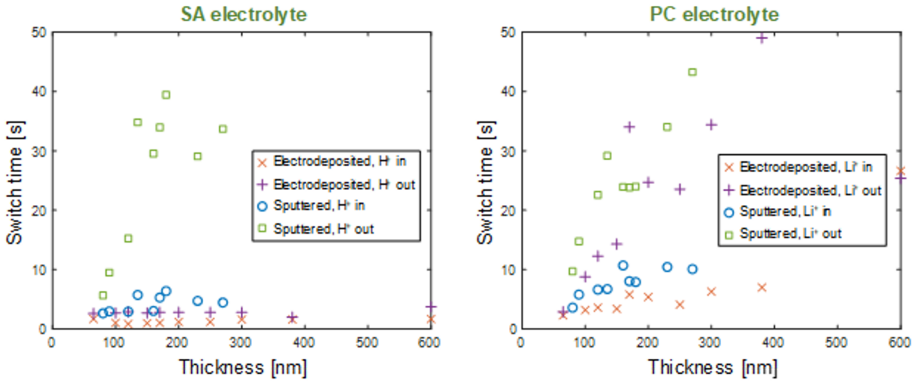

Figure 4.12: Switching time from bright to dark and dark to bright for electrodeposited and sputtered films vs thickness in sulfuric acid and propylene carbonate. Adapted from Paper III.

In both electrolytes, the switching time of the electrodeposited films was always lower than for the sputtered ones. We attributed this to the morphology of the film. Porous and rough films favor fast intercalation of ions [85]. The speed was significantly influenced by the electrolyte: in sulfuric acid, all films switched fast (a few seconds) apart from the sputtered ones from dark to bright which took one order of magnitude longer. In propylene carbonate, all the films, in both switching directions, took tens of seconds to switch.
Lastly, we fabricated the nanostructures presented in paper II with electrodeposited WO_3 and we characterized them in propylene carbonate. Figure 4.13 A shows the CIE diagram of 3 nanostructures with 200 nm, 300 nm, and 400 nm electrodeposited WO_3. Compared with the results in paper II, the color gamut was slightly smaller, which could be attributed to the rougher surface of the electrochromic material which broadens the cavity resonance. Despite this, the color quality was still good compared to commercial alternatives [86]. Figure 4.13 B shows the spectra of the 300 nm WO_3 cavity corresponding to the bright, dark, and one of the intermediate states of WO_3. The colors of the lines correspond to the pseudo colors calcu-

lated from the spectra, showing that the cavity could reflect green, blue, and purple colors. The most remarkable improvement in using electrodeposited WO_3 concerned the switching speed. Figure 4.13 C shows the intensity vs time at 630 nm for cavities with electrodeposited and sputtered films. The electrodeposited one showed a switching time of less than 10 s compared to several minutes for the sputtered films. The number of nanoholes on the backside of the structures (see Figure 4.13 D) could also influence the speed. However, we assumed that the same number of nanoholes, on average, was present in both structures and that the difference was only due to the properties of the WO_3 films.

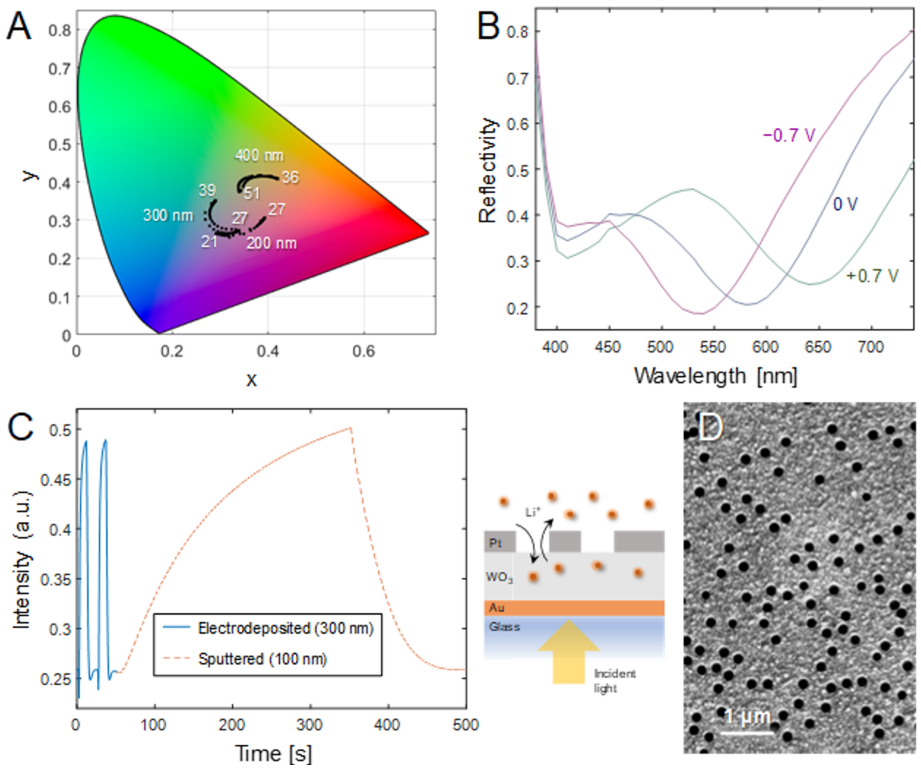

Figure 4.13: Electrochromic nanostructures with electrodeposited WO_3. A) CIE diagram and Y values (bright and dark state of WO_3) of 3 structures with different thicknesses of WO_3. B) Reflectivity spectra of the nanostructure with 300 nm WO_3 corresponding to dark, bright and intermediate state of WO_3. C) Switching dynamics of nanostructures with electrodeposited and sputtered films (at 630 nm). D) SEM image of the backside of the nanostructures with electrodeposited WO_3. Reproduced from Paper III.

4.5 Contrast enhancement in the blue region

In Paper IV we considered a different organic alternative to implement on the blue metasurfaces presented in Paper I: poly-dimethylpropylenedioxypyrrole (pProDOP). This polymer has been reported to show high optical contrast in the blue region [87]. Figure 4.14 shows an SEM image of a blue metasurface (on the left), comprised of aluminum, aluminum oxide and gold films. The array of nanoholes is visible on the top gold film. On the right, the same metasurface with pProDOP electrodeposited on the top gold film.

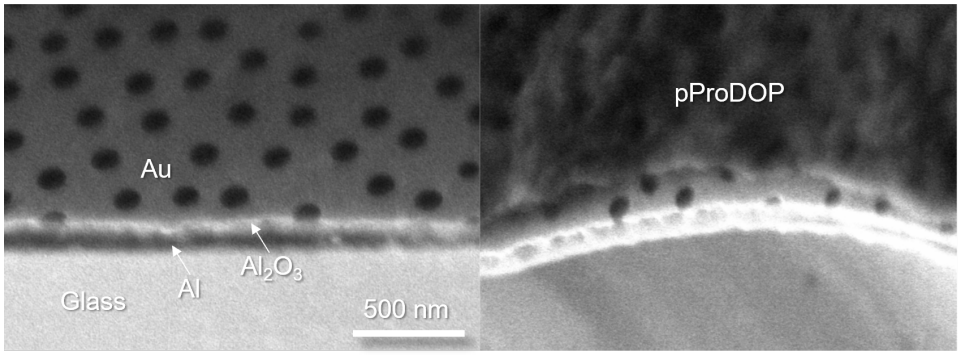

Figure 4.14: SEM images of a blue metasurface with pProDOP. Reported from Paper IV.

In the bright state, the polymer film did not influence the peak position, maintaining the desired color of the metasurface. The reflectivity was affected, however not significantly more than for $pProDOTMe_2$ evaluated in Paper I. The contrast, on the other hand, was improved and reached over 50%.

Chapter 5

Results not yet published

5.1 Structural colors on active matrix

One step forward toward a display prototype is the implementation of the structural colors and the electrochromic materials on a matrix. In this section we show the fabrication of the metasurfaces presented in Paper I onto TFT arrays. However, we will not cover the individual addressing of the pixels since that was not done by the author of this thesis. The arrays were purchased from Plastic Logic and consisted of 200x200 μm^2 pixels onto a flexible PET substrate. The fabrication of the metasurfaces on the TFT substrate was carried out using multiple lithography steps, as shown in Figure 5.1. The flexible substrate was placed on a silicon wafer using thermal tape (releasing at 120°C) to keep the surface flat, especially during the laser lithography steps. During lift-off in acetone, the glue of the tape would dissolve and affect the adhesion of the substrate to the silicon wafer. Hence, the tape was completely removed by heating the wafer to 120 °C for a few seconds and the substrate was placed on the wafer again with a new piece of tape. This was done after every lift-off step. Because the substrate was PET, it was not possible to leave the silicon wafer on the hot plate for a prolonged period of time, as this would cause the plastic to degrade. The substrate was heated for a few seconds several times, allowing it to cool between each step until it could be removed completely. For the same reason, the soft baking of the resist had to be carried out at a lower temperature, 85°C for 5 minutes, instead of 140°C for 1 minute as in the standard recipe.

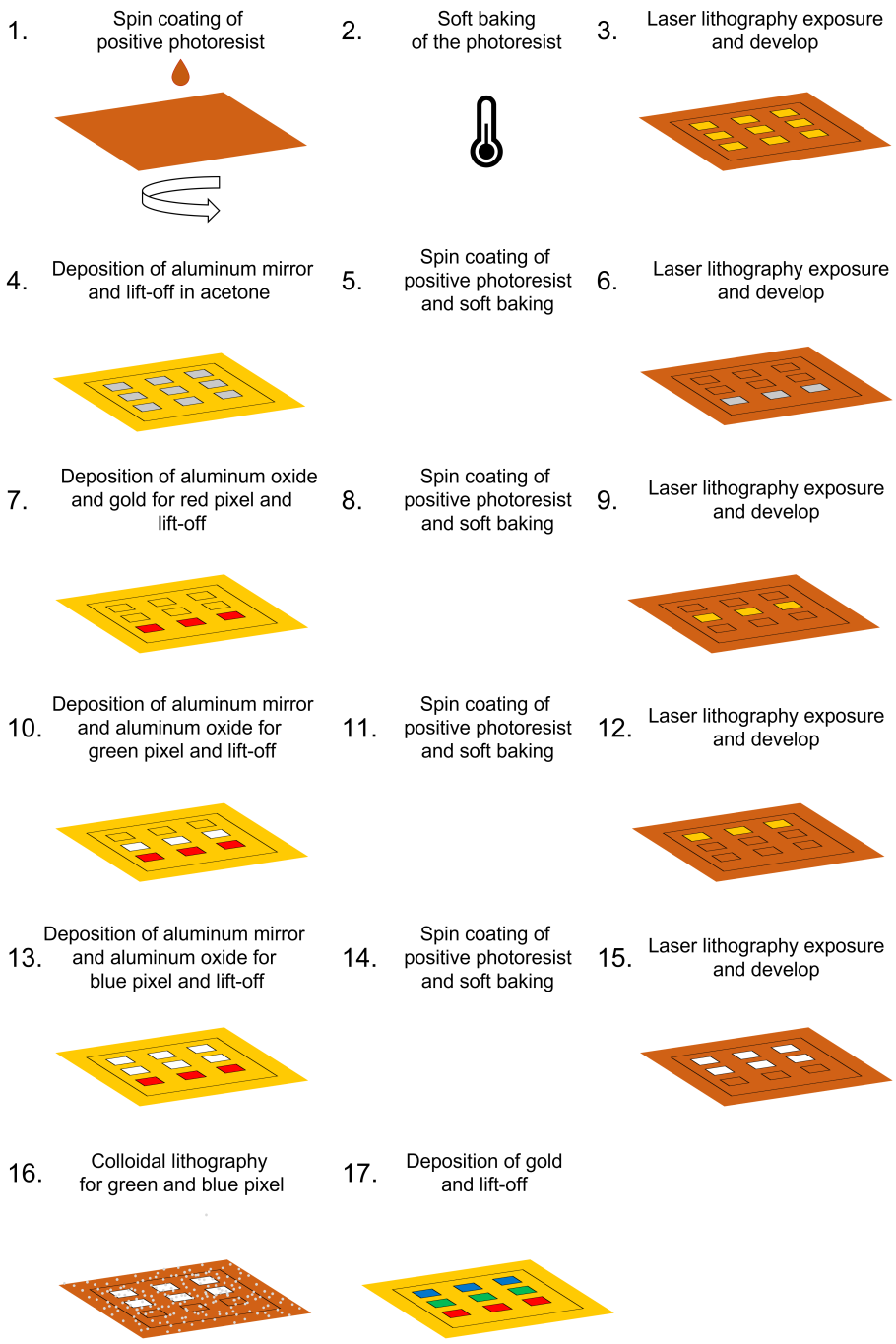

Figure 5.1: Schematic of lithography and thin film deposition steps for the fabrication of RGB metasurfaces on commercial TFT arrays.

First, the photoresist was spin coated and soft baked. Then all the pixels were exposed and, after the photoresist development, the 100 nm aluminum mirror, common to all the colored structures, was evaporated. Lift-off was carried out in acetone and the thermal tape was removed and reapplied. Then, the red pixels were exposed and the whole structure was evaporated and completed (61 nm of Al_2O_3 and 20 nm Au), the result is shown in Figure 5.2 A. After lift-off, the green pixels were exposed and 95 nm of Al_2O_3 was evaporated. The same was carried out for the blue pixel with 110 nm of Al_2O_3. The green and blue pixels were then exposed simultaneously to perform colloidal lithography, then 20 nm Au was evaporated to complete the structures. After lift-off and removal of the thermal tape, all the RGB structures were completed on the TFT and the result can be seen in Figure 5.2 B.

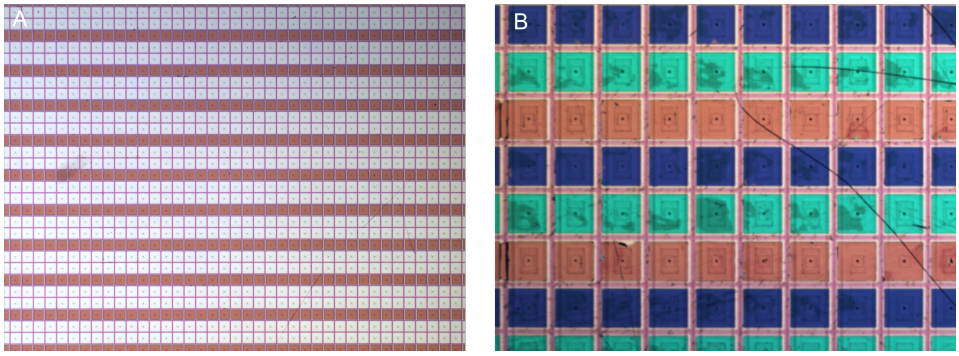

Figure 5.2: Structural colors on TFT arrays. A) Red metasurface fabricated onto the array (step 7 in Figure 5.1). B) RGB metasurfaces fabricated onto the array (step 17 in Figure 5.1).

5.2 Towards cleanroom-free fabrication

5.2.1 Electroless deposition of gold

Electroless deposition of a thin gold film was attempted on both glass and WO_3. The approach was the same in both scenarios: synthesis of nanoparticles, anchoring of nanoparticles using 3-aminopropylsilatrane (APS) on the substrate, and merging of nanoparticles in a solution containing gold ions [88, 76] to form a continuous film (Figure 5.3).

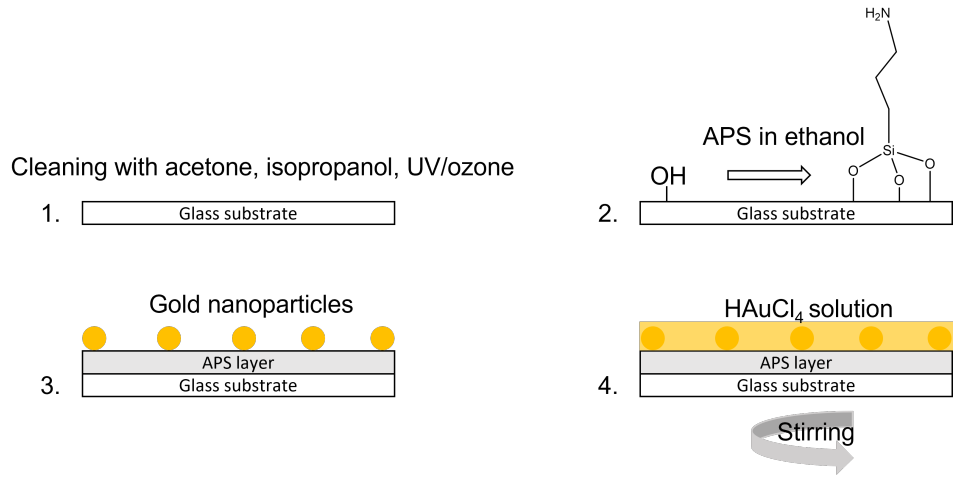

Figure 5.3: Schematic of gold nanoparticles anchoring onto a glass substrate using APS.

First, the gold nanoparticles were synthesized by sodium citrate reduction of $HAuCl_4$ using a 4:1 ratio, aiming at a diameter of around 12 nm [89]. In Figure 5.4, an SEM image of the particles on glass shows that the particles had diameters around 15-20 nm.

The glass was cleaned with acetone and isopropanol and finally with 20 minutes of UV/Ozone. The last step not only cleans any residues of organic material on the surface but also functionalizes it with -OH groups on which APS (0.460 mM in ethanol) can bond [90]. After the functionalization of the glass surface with the silatrane, the substrate was immersed in the gold nanoparticles solution overnight, where they could electrostatically attach to the amine groups. After overnight soaking the excess nanoparticles solution was rinsed with MilliQ water and the substrate was immersed in the gold ion solution made of 10 ml of 0.01% $HAuCl_4$ and 500 µl of 30 % H_2O_2, which was continuously agitated. The merging step was done for 12 minutes and 22 minutes, however, the resulted films were not uniform, with a gold color at the edges and a pink tint in the center (Figure 5.4 A) which indicated that there still was plasmonic activity, hence the particles were still separated. This was confirmed by the SEM images in Figure 5.4 C and D, which show the non-merged particles in the corner and at the edge of the sample respectively. Since the gold films were meant to be used as electrodes for subsequent electrodeposition of WO_3, adhesion to the glass substrate and

conductivity were tested. Tape was used to test the adhesion of the film [76] and regardless of the pressure applied to place the tape and the speed used to remove it, no visible peeling off of the gold film was observed. However, clamping with a crocodile-like clamp or handling with gloves would destroy the film, leaving exposed glass after removal. Moreover, none of the fabricated samples were conductive. Hence, the gold films could not be used as electrodes for electrodeposition of WO_3. An attempt to increase the adhesion to the glass substrate was to anneal the gold nanoparticles, already deposited on glass, at 600°C for 10 hours (5°C per minute rate) [91]. This did indeed improve the adhesion, however, after the merging step, the films were still not uniform and not conductive. This was probably related to the particles not being completely merged into a uniform film like we observed for non-annealed samples. Further work is needed toward a more uniform film with good adhesion and conductivity.

Following the same procedure, we attempted to deposit the gold nanoparticles on WO_3, however, the nanoparticles solution would destroy the WO_3 film. This was attributed to the presence of the reducing agent which would reduce the WO_3 and dissolve it. This was tested by immersing a WO_3 film in a sodium citrate solution and $HAuCl_4$ separately. The latter did not affect the film, but the former did. To overcome the issue, centrifuging the solution and diluting it with MilliQ was tried, but the solution would still dissolve the WO_3 film eventually. Different methods for synthesis of the nanoparticles could be tried to avoid the reduction of WO_3, for example by using microwave-assisted synthesis from $HAuCl_4$ in water [92].

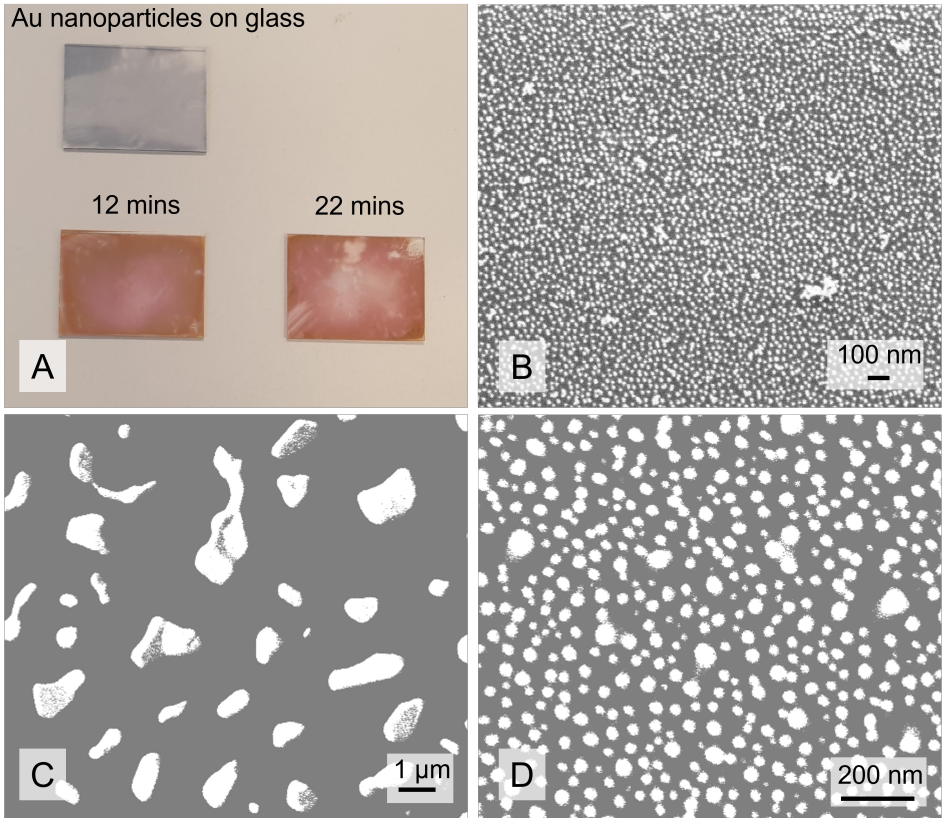

Figure 5.4: Gold nanoparticles synthetized with 4:1 ratio sodium citrate - $HAuCl_4$ deposited on glass (18x24 mm^2). A) Particles on glass and after 12 minutes and 22 minutes of merging in the gold ions solution. B) SEM image of the Au nanoparticles on glass. SEM picture of the corner (C) and edge (D) of a sample after the merging step.

5.2.2 Electrodeposition of platinum

Platinum was electrodeposited onto gold nanoparticles coated ITO substrates using a three-electrodes setup. The electrolyte was comprised of 17 mM $2PtCl_6$ and 250 mM Na_2HPO_4 [93] and was kept on magnetic stirring overnight before being used. The deposition was carried out using a 0.1 s pulse at -0.4 V followed by a 0.1 s delay at open circuit, for several cycles. The coating of ITO with gold nanoparticles was carried out as described in Subsection 5.2.1 and improved the adhesion of the films onto the ITO glass, which would otherwise be removed by simple handling with gloves. The films appeared smooth and polished, however, after a certain thickness, the film would just leave the surface of the ITO to the deposition solution. The platinum electrodes were however tested for electrodeposition of WO_3. The deposition could not be carried out due to the platinum film leaving the ITO as soon as a negative potential in the WO_3 deposition solution was applied. When using an evaporated platinum film, the deposition could be carried out, hence the reason seemed to lie in the deposition method.

Chapter 6

Conclusion

In this work, we have presented several steps toward an improved reflective display device. In paper I, we have shown the fabrication of red, green, and blue surfaces based on Fabry-Perót cavities which showed high chromaticity and reflectivity. Furthermore, they were stable in non-aqueous electrolytes, which are commonly used when implementing electrochromic materials on top of the structures. Two electrochromic materials have been investigated for deposition on top of colored surfaces to allow on and off states: $pProDOTMe_2$ and WO_3. The inorganic option showed the highest reflectivity modulation, up to 60%, while the organic option was superior in terms of switching speed, less than 1 s. Both materials showed low power consumption and could, in principle, outperform existing electrophoretic displays in terms of image quality if implemented in a real device.

In Paper II, we proposed a novel design for structural colors, based on WO_3 sandwiched between gold and platinum thin films, that exhibited a wide color range. The design also allowed the electrochemical cell to be placed behind the colored surface, resulting in high reflectivity for a device configuration. Two structures could be combined to generate all colors. Comparing this to a real device, which requires 3 pixels, the performance improves. We showed this by comparing the dual dynamic pixels configuration with the latest device on the market. As far as brightness and chromaticity are concerned, our nanostructures could outperform it.

In Paper III, we considered the possible improvement of the nanostructures presented in Paper II by the implementation of WO_3 deposited via electrochemistry. A systematic comparison was made between electrodeposited and sputtering films. Electrodeposition is an inexpensive and simple process that could produce films with high optical modulation and switch-

ing speeds. As a matter of fact, we found that one of the major differences between the two methods was the switching speed of electrodeposited films, which was higher. This was attributed to the rough and porous morphology of the films, which promoted the intercalation of ions. Very high contrast could be achieved for both methods (up to 98% in red) in the aqueous electrolyte. However, sulfuric acid adversely affected the material's lifetime, unlike propylene carbonate. For sputtered films, up to 93% optical modulation could be achieved in the organic electrolyte, which provide longer stability. Electrodeposited films performed slightly worse in propylene carbonate, showing a contrast up to 87%. As a final step, we fabricated the nanostructures presented in Paper II with electrodeposited WO_3. More than one order of magnitude improvement in switching speed was observed due to the porous morphology of the films.

Based on the concept of facile fabrication of the nanostructures, we considered the electroless deposition of gold films and the electrodeposition of platinum films. Electroless gold films were deposited by merging gold nanoparticles anchored to glass substrates. The films, however, proved neither uniform nor conductive. In addition, platinum films showed poor quality and were not suitable for use as electrodes for the deposition of WO_3.

Lastly, we explored an additional organic material, pProDOP, to enhance the contrast of the blue metasurfaces. The polymer showed over 50% contrast in the blue region, higher than the pProDOTMe$_2$ evaluated in Paper I.

Chapter 7

Outlook

Throughout this work, various methods are presented for fabricating bright and colorful pixels. If we look back at the introduction chapter, this was one of the issues with commercial reflective displays available nowadays. However, more work is required to achieve a fully working display that can compete with the commercially available options.

In Paper I, we showed how electrochromic materials can be used in combination with colored pixels. The three subpixels are still necessary for this design, but greyscale and on/off states can be achieved. In Paper II, we showed a dynamic pixel design where the division could be limited to two subpixels, thereby reducing the losses that occur in the conventional RGB structure. Despite the fact that some states are whiter than others, possibly leading to a grayscale, these pixels could not show perfect on and off states. It is a big challenge to address this issue. Is there a way to have a monopixel that can also be switched on and off? The mechanisms for adjusting color and on/off should be separate. Ideally, the color could be tuned without any loss of brightness and the on/off mechanism could be independently controlled. Recent years have seen reversible metal deposition gain interest for light modulation [94, 95] and could be investigated in conjunction with our metasurfaces to achieve a separate control of the reflectivity. This is, however, not easily done since it would require an implementation of the reversible mirror so that its dissolution/deposition only happens after a threshold voltage. Even in that case, it would not be possible to modulate the reflectivity for a dynamic pixel whose color is directly related to the applied voltage.

It would also be necessary to improve the switching speed. For commercial devices, the refresh rate is definitely a problem. In Paper IV, the

electrodeposited films showed improved switching speed. However, for human eyes to perceive motion, the refresh rate must reach at least 20 Hz [68].

Lastly, section 5.1 outlined preliminary results on device fabrication, but individual addressing of the pixels is required to either electrodeposit or control the individual pixels for dynamic images.

Acknowledgements

I would like to thank the Swedish Foundation for Strategic Research for its financial support as well as MyFab Chalmers, where part of this work was performed. I thank my supervisor Andreas Dahlin for the support and guidance, my co-supervisor Per Rudquist and my examiner Christian Müller for the useful discussions and the feedback on this thesis. Thank you to all my colleagues, especially to my closest ones in Andreas Dahlin's group. A special thanks to Oliver Olsson, who has supported me in my research and in my daily life, as well as to my office mates Roujin Ghaffari and Robin Nilsson who have eased my days as a PhD student. Finally, thank you to my parents. I am very grateful for all you have done for me.

Bibliography

[1] Kunli Xiong et al. “Active control of plasmonic colors: emerging display technologies”. In: *Reports on Progress in Physics* 82.2 (2019), p. 024501.

[2] Cristian Talens-Estarelles et al. “Use of digital displays and ocular surface alterations: a review”. In: *The Ocular Surface* 19 (2021), pp. 252–265.

[3] Gianluca Tosini, Ian Ferguson, and Kazuo Tsubota. “Effects of blue light on the circadian system and eye physiology”. In: *Molecular Vision* 22 (2016), p. 61.

[4] Marıa Rodrıguez Fernández, Eduardo Zalama Casanova, and Ignacio González Alonso. “Review of display technologies focusing on power consumption”. In: *Sustainability* 7.8 (2015), pp. 10854–10875.

[5] Simone Benedetto et al. “E-readers and visual fatigue”. In: *PLOS ONE* 8.12 (2013), e83676.

[6] Jason Heikenfeld et al. “A critical review of the present and future prospects for electronic paper”. In: *Journal of the Society for Information Display* 19.2 (2011), pp. 129–156.

[7] Marika Gugole et al. “High-contrast switching of plasmonic structural colors: inorganic versus organic electrochromism”. In: *ACS Photonics* 7.7 (2020), pp. 1762–1772.

[8] Cyril Hilsum. “Flat-panel electronic displays: a triumph of physics, chemistry and engineering”. In: *Philosophical Transactions of the Royal Society A: Mathematical, Physical and Engineering Sciences* 368.1914 (2010), pp. 1027–1082.

[9] DJ Robbins. “The cathode-ray tube—Why it will not go away”. In: *Microelectronics Journal* 11.3 (1980), pp. 10–23.

[10] LK Anderson. "The cathode ray tube display: Why use anything else?" In: *Journal of Vacuum Science and Technology* 10.5 (1973), pp. 761–767.

[11] JP Boeuf. "Plasma display panels: physics, recent developments and key issues". In: *Journal of Physics D: Applied Physics* 36.6 (2003), R53.

[12] David E Mentley. "State of flat-panel display technology and future trends". In: *Proceedings of the IEEE* 90.4 (2002), pp. 453–459.

[13] Larry F Weber. "History of the plasma display panel". In: *IEEE transactions on Plasma Science* 34.2 (2006), pp. 268–278.

[14] Hai-Wei Chen et al. "Liquid crystal display and organic light-emitting diode display: present status and future perspectives". In: *Light: Science & Applications* 7.3 (2018), pp. 17168–17168.

[15] Matthias Bremer et al. "The TV in your pocket: development of liquid-crystal materials for the new millennium". In: *Angewandte Chemie International Edition* 52.34 (2013), pp. 8880–8896.

[16] Robert H Chen. *Liquid crystal displays: fundamental physics and technology*. John Wiley & Sons, 2011.

[17] Dirk Hertel and John Penczek. "Predicting the viewing direction performance of e-paper displays with front light under ambient lighting conditions". In: *Journal of the Society for Information Display* 23.11 (2015), pp. 510–522.

[18] Janglin Chen, Wayne Cranton, and Mark Fihn. *Handbook of Visual Display Technology. [electronic resource]*. Springer Berlin Heidelberg, 2019. ISBN: 9783642359477.

[19] Mi-Ji Kim, Gimin Sung, Jeong-Yun Sun, et al. "Stretchable and reflective displays: materials, technologies and strategies". In: *Nano Convergence* 6.1 (2019), pp. 1–24.

[20] Peng Fei Bai et al. "Review of paper-like display technologies (invited review)". In: *Progress in Electromagnetics Research* 147 (2014), pp. 95–116.

[21] Yi Lu et al. "Progress in Advanced Properties of Electrowetting Displays". In: *Micromachines* 12.2 (2021), p. 206.

[22] J Heikenfeld et al. "Electrofluidic displays using Young–Laplace transposition of brilliant pigment dispersions". In: *Nature Photonics* 3.5 (2009), pp. 292–296.

[23] Peter Andersson Ersman, Jun Kawahara, and Magnus Berggren. "Printed passive matrix addressed electrochromic displays". In: *Organic Electronics* 14.12 (2013), pp. 3371–3378.

[24] D-K Yang et al. "Control of reflectivity and bistability in displays using cholesteric liquid crystals". In: *Journal of Applied Physics* 76.2 (1994), pp. 1331–1333.

[25] DH Sliney. "What is light? The visible spectrum and beyond". In: *Eye* 30.2 (2016), pp. 222–229.

[26] Andrzej Grzybowski and Konrad Kupidura-Majewski. "What is color and how it is perceived?" In: *Clinics in Dermatology* 37.5 (2019), pp. 392–401.

[27] Michael Tri Hoang Do and King-Wai Yau. "Intrinsically photosensitive retinal ganglion cells". In: *Physiological reviews* 90.40 (2010), pp. 1547–1581.

[28] Tiffany M Schmidt, Shih-Kuo Chen, and Samer Hattar. "Intrinsically photosensitive retinal ganglion cells: many subtypes, diverse functions". In: *Trends in Neurosciences* 34.11 (2011), pp. 572–580.

[29] Andrew Stockman. "Cone fundamentals and CIE standards". In: *Current Opinion in Behavioral Sciences* 30 (2019), pp. 87–93.

[30] Marcelo Bertalmıo. *Vision models for high dynamic range and wide colour gamut imaging: techniques and applications*. Academic Press, 2019.

[31] John Guild. "The colorimetric properties of the spectrum". In: *Philosophical Transactions of the Royal Society of London. Series A, Containing Papers of a Mathematical or Physical Character* 230.681-693 (1931), pp. 149–187.

[32] Hugh S Fairman, Michael H Brill, and Henry Hemmendinger. "How the CIE 1931 color-matching functions were derived from Wright-Guild data". In: *Color Research & Application* 22.1 (1997), pp. 11–23.

[33] William David Wright. "A re-determination of the trichromatic coefficients of the spectral colours". In: *Transactions of the Optical Society* 30.4 (1929), p. 141.

[34] Thomas Smith and John Guild. "The CIE colorimetric standards and their use". In: *Transactions of the Optical Society* 33.3 (1931), p. 73.

[35] Glenn A Fry. “Amalgamation of the wright and guild color-mixture data”. In: *Color Research & Application* 13.1 (1988), pp. 50–54.

[36] WS Stiles and JM Burch. “Interim report to the commission internationale de l’éclairage, Zurich, 1955, on the National Physical Laboratory’s investigation of colour-matching (1955)”. In: *Optica Acta: International Journal of Optics* 2.4 (1955), pp. 168–181.

[37] Johannes J Vos. “Colorimetric and photometric properties of a 2 fundamental observer”. In: *Color Research & Application* 3.3 (1978), pp. 125–128.

[38] JS Setchell Jr. “Colour description and communication”. In: *Colour Design*. Elsevier, 2012, pp. 219–253.

[39] Jian Wei Xu, Ming Hui Chua, and Kwok Wei Shah. *Electrochromic smart materials: fabrication and applications*. Royal Society of Chemistry, 2019.

[40] Claes G Granqvist. *Handbook of inorganic electrochromic materials*. Elsevier, 1995.

[41] IF Chang, BL Gilbert, and TI Sun. “Electrochemichromic systems for display applications”. In: *Journal of The Electrochemical Society* 122.7 (1975), p. 955.

[42] Paul Monk, Roger Mortimer, and David Rosseinsky. *Electrochromism and electrochromic devices*. Cambridge University Press, 2007.

[43] SK Deb. “Optical and photoelectric properties and colour centres in thin films of tungsten oxide”. In: *Philosophical Magazine* 27.4 (1973), pp. 801–822.

[44] Neil W Ashcroft, N David Mermin, and Neil W Ashcroft. *Solid state physics*. 1976.

[45] G Hollinger, Tran Minh Duc, and A Deneuville. “Charge Transfer in Amorphous Colored W O 3 Films Observed by X-Ray Photoelectron Spectroscopy”. In: *Physical Review Letters* 37.23 (1976), p. 1564.

[46] Satyen K Deb. “Opportunities and challenges in science and technology of WO_3 for electrochromic and related applications”. In: *Solar Energy Materials and Solar Cells* 92.2 (2008), pp. 245–258.

[47] Lars Berggren, Andris Azens, and Gunnar A Niklasson. “Polaron absorption in amorphous tungsten oxide films”. In: *Journal of Applied Physics* 90.4 (2001), pp. 1860–1863.

[48] Malin B Johansson et al. "Optical properties of nanocrystalline WO_3 and WO_3-x thin films prepared by DC magnetron sputtering". In: *Journal of Applied Physics* 115.21 (2014), p. 213510.

[49] Brian W Faughnan, Richard S Crandall, Philip M Heyman, et al. "Electrochromism in WO_3 amorphous films". In: *RCA Rev* 36.1 (1975), pp. 177–197.

[50] MF Saenger et al. "Polaron and phonon properties in proton intercalated amorphous tungsten oxide thin films". In: *Physical Review B* 78.24 (2008), p. 245205.

[51] Eric Bousquet et al. "First-principles characterization of single-electron polaron in WO_3". In: *Physical Review Research* 2.1 (2020), p. 012052.

[52] Jesper Ederth et al. "Small polaron formation in porous WO_3-x nanoparticle films". In: *Journal of Applied Physics* 96.10 (2004), pp. 5722–5726.

[53] Lev Davidovich Landau. "Electron motion in crystal lattices". In: *Phys. Z. Sowjet.* 3 (1933), p. 664.

[54] Carlos A Triana, Claes-Göran Granqvist, and Gunnar A Niklasson. "Electrochromism and small-polaron hopping in oxygen deficient and lithium intercalated amorphous tungsten oxide films". In: *Journal of Applied Physics* 118.2 (2015), p. 024901.

[55] Jiyu Sun, Bharat Bhushan, and Jin Tong. "Structural coloration in nature". In: *RSC Advances* 3.35 (2013), pp. 14862–14889.

[56] Andrew Richard Parker. "515 million years of structural colour". In: *Journal of Optics A: Pure and Applied Optics* 2.6 (2000), R15.

[57] S Kinoshita, Shinya Yoshioka, and J Miyazaki. "Physics of structural colors". In: *Reports on Progress in Physics* 71.7 (2008), p. 076401.

[58] Stéphanie M Doucet and Melissa G Meadows. "Iridescence: a functional perspective". In: *Journal of The Royal Society Interface* 6.suppl_2 (2009), S115–S132.

[59] Doekele G Stavenga. "Thin film and multilayer optics cause structural colors of many insects and birds". In: *Materials Today: Proceedings* 1 (2014), pp. 109–121.

[60] Eugene Hecht. *Optics. [electronic resource].* Pearson custom library. Pearson, 2014. ISBN: 1292034807.

[61] Andreas B Dahlin. "Plasmonic biosensors: an integrated view of refractometric detection". In: (2012).

[62] Francis Arthur Jenkins and Harvey Elliott White. "Fundamentals of optics". In: *Indian Journal of Physics* 25 (1957), pp. 265–266.

[63] Stefan A Maier et al. *Plasmonics: fundamentals and applications*. Vol. 1. Springer, 2007.

[64] Mark L Brongersma and Pieter G Kik. *Surface plasmon nanophotonics*. Vol. 131. Springer, 2007.

[65] Jiřı Homola. "Surface plasmon resonance sensors for detection of chemical and biological species". In: *Chemical Reviews* 108.2 (2008), pp. 462–493.

[66] Heinz Raether. "Surface plasmons on gratings". In: *Surface plasmons on smooth and rough surfaces and on gratings*. Springer, 1988, pp. 91–116.

[67] Kunli Xiong et al. "Plasmonic metasurfaces with conjugated polymers for flexible electronic paper in color". In: *Advanced Materials* 28.45 (2016), pp. 9956–9960.

[68] Kunli Xiong et al. "Video Speed Switching of Plasmonic Structural Colors with High Contrast and Superior Lifetime". In: *Advanced Materials* 33.41 (2021), p. 2103217.

[69] Marıa Rodrıguez Fernández, Eduardo Zalama Casanova, and Ignacio González Alonso. "Review of display technologies focusing on power consumption". In: *Sustainability* 7.8 (2015), pp. 10854–10875.

[70] Allen J. Bard and Larry R. Faulkner. *Electrochemical methods : fundamentals and applications*. Wiley, 2001. ISBN: 0471043729.

[71] Noémie Elgrishi et al. "A practical beginner's guide to cyclic voltammetry". In: *Journal of Chemical Education* 95.2 (2018), pp. 197–206.

[72] John E Mahan. *Physical vapor deposition of thin films*. Wiley, 2000.

[73] Milton Ohring, Sohrab Zarrabian, and Austin Grogan. "The materials science of thin films". In: (1992).

[74] Lawrence T Lamont Jr and Frederick T Turner. "The role of dc self-bias potential in the control of rf sputtering". In: *Journal of Vacuum Science and Technology* 11.1 (1974), pp. 47–51.

[75] Guofa Cai et al. "Ultra-large optical modulation of electrochromic porous WO_3 film and the local monitoring of redox activity". In: *Chemical Science* 7.2 (2016), pp. 1373–1382.

[76] Per Hanarp et al. “Control of nanoparticle film structure for colloidal lithography”. In: *Colloids and Surfaces A: Physicochemical and Engineering Aspects* 214.1-3 (2003), pp. 23–36.

[77] Markku Tilli et al. *Handbook of silicon based MEMS materials and technologies*. Elsevier, 2020.

[78] Kannan M Krishnan. *Principles of Materials Characterization and Metrology*. Oxford University Press, 2021.

[79] Anwar Ul-Hamid. *A beginners' guide to scanning electron microscopy*. Vol. 1. Springer, 2018.

[80] Kunli Xiong et al. “Switchable plasmonic metasurfaces with high chromaticity containing only abundant metals”. In: *Nano Letters* 17.11 (2017), pp. 7033–7039.

[81] Zhen Wang et al. “Towards full-colour tunability of inorganic electrochromic devices using ultracompact fabry-perot nanocavities”. In: *Nature Communications* 11.1 (2020), pp. 1–9.

[82] Yohan Lee et al. “Full-color-tunable nanophotonic device using electrochromic tungsten trioxide thin film”. In: *Nano Letters* 20.8 (2020), pp. 6084–6090.

[83] Eric Hopmann and Abdulhakem Y Elezzabi. “Plasmochromic nanocavity dynamic light color switching”. In: *Nano Letters* 20.3 (2020), pp. 1876–1882.

[84] Claes Göran Granqvist et al. “Electrochromic materials and devices for energy efficiency and human comfort in buildings: A critical review”. In: *Electrochimica Acta* 259 (2018), pp. 1170–1182.

[85] Keon-Woo Kim et al. “Extremely fast electrochromic supercapacitors based on mesoporous WO_3 prepared by an evaporation-induced self-assembly”. In: *NPG Asia Materials* 12.1 (2020), pp. 1–10.

[86] Marika Gugole et al. “Electrochromic Inorganic Nanostructures with High Chromaticity and Superior Brightness”. In: *Nano Letters* 21.10 (2021), pp. 4343–4350.

[87] Philippe Schottland et al. “Poly (3, 4-alkylenedioxypyrrole) s: Highly stable electronically conducting and electrochromic polymers”. In: *Macromolecules* 33.19 (2000), pp. 7051–7061.

[88] Jiandong Hu et al. “Novel plating solution for electroless deposition of gold film onto glass surface”. In: *Surface and Coatings Technology* 202.13 (2008), pp. 2922–2926.

[89] Nidhi Nath and Ashutosh Chilkoti. "Label-free biosensing by surface plasmon resonance of nanoparticles on glass: optimization of nanoparticle size". In: *Analytical Chemistry* 76.18 (2004), pp. 5370–5378.

[90] Mario F Heinig et al. "Aminopropylsilatrane linkers for easy and fast fabrication of high-quality 10 nm thick gold films on SiO2 substrates". In: *ACS Applied Nano Materials* 3.5 (2020), pp. 4418–4427.

[91] Tanya Karakouz et al. "Stabilization of gold nanoparticle films on glass by thermal embedding". In: *ACS Applied Materials & Interfaces* 3.4 (2011), pp. 978–987.

[92] C Vargas-Hernandez et al. "A synthesis route of gold nanoparticles without using a reducing agent". In: *Applied Physics Letters* 96.21 (2010), p. 213115.

[93] John J Whalen, James D Weiland, and Peter C Searson. "Electrochemical deposition of platinum from aqueous ammonium hexachloroplatinate solution". In: *Journal of the Electrochemical Society* 152.11 (2005), p. C738.

[94] Cheon Woo Moon, Youngji Kim, and Jerome Kartham Hyun. "Active electrochemical high-contrast gratings as on/off switchable and color tunable pixels". In: *Nature Communications* 13.1 (2022), pp. 1–8.

[95] Chihyun Park et al. "Switchable silver mirrors with long memory effects". In: *Chemical science* 6.1 (2015), pp. 596–602.